A crossed-beam experiment on intramultiplet mixing collisions with short-lived Ne** {(2p)5(3p)} atoms

A crossed-beam experiment on intramultiplet mixing collisions with short-lived Ne** $\{(2p)^5(3p)\}$ atoms

M. P. I. Manders, W. M. Ruyten, F. V. D. Beucken, J. P. J. Driessen, W. J. T. Veugelers, P. H. Kramer, E. J. D. Vredenbregt, W. B. M. van Hoek, G. J. Sandker, H. C. W. Beijerinck, and B. J. Verhaar

Citation: The Journal of Chemical Physics **89**, 4777 (1988); doi: 10.1063/1.455672
View online: http://dx.doi.org/10.1063/1.455672
View Table of Contents: http://aip.scitation.org/toc/jcp/89/8
Published by the American Institute of Physics

A crossed-beam experiment on intramultiplet mixing collisions with short-lived Ne** $\{(2p)^5(3p)\}$ atoms

M. P. I. Manders, W. M. Ruyten, F. v. d. Beucken, J. P. J. Driessen, W. J. T. Veugelers, P. H. Kramer, E. J. D. Vredenbregt, W. B. M. van Hoek, G. J. Sandker, H. C. W. Beijerinck, and B. J. Verhaar

Physics Department, Eindhoven University of Technology, P. O. Box 513, 5600 MB Eindhoven, The Netherlands

(Received 2 June 1988; accepted 6 July 1988)

We describe the design, operation, and calibration of a crossed-beam experiment for the study of intramultiplet mixing collisions of short-lived electronically excited $Ne\{(2p)^5(3p)\} \equiv \{\alpha\}$ atoms with ground-state atoms/molecules. The excellent performance of almost 1 kHz/Å^2 (number of counts per unit of inelastic cross section) enables us to measure, with good accuracy, absolute total Ne**–X cross sections $Q_{l\leftarrow k}^{|M_k|}$, for the $\{\alpha\}_k \rightarrow \{\alpha\}_l$ transition. Here M_k is the magnetic quantum number of the electronic angular momentum **J** of the initial $\{\alpha\}_k$ state with respect to the asymptotic relative velocity. The polarized $\{\alpha\}_k$ state is produced with a polarized laser. Narrow-band interference filters are used to detect the fluorescence radiation from the short-lived $\{\alpha\}_k$ and $\{\alpha\}_l$ states. An extensive series of measurements has been undertaken to calibrate the experiment. These are related to, e.g., beam properties, the optical-pumping process, and the optical detection system. The basic principles of the collision experiment itself have been thoroughly examined as well. We discuss the kinds of experiments it is possible to perform. These have yielded absolute (within 30%) cross sections between 0.05 and 50 Å^2. Very strong polarization effects have been observed, with $0.1 \lesssim Q_{l\leftarrow k}^{|0|}/Q_{l\leftarrow k}^{|1|} \lesssim 10$. The average collision energy has been varied between 50 and 250 meV (depending to some extent on the collision partner), by using a seeded primary beam and by manipulating the Newton diagram of primary- and secondary-beam velocity vectors. Time-of-flight measurements with a laser chopper have been performed as well. The wide range of Ne**-collision partners offers the option of studying intramultiplet mixing pure (He, Ne), and in conjunction with Penning ionization (noble gas atoms Ar, Kr, Xe) or even angular-momentum coupling and anisotropy effects (molecules, from H_2 to CO_2, N_2O).

I. INTRODUCTION

The study of inelastic collisions of atoms in short-lived, electronically excited states offers both great potential rewards and considerable practical difficulties. The latter have made this subject a relatively new entry in the atomic-collisions field. The former have caused a sizable body of literature to appear in recent years, both of a theoretical[1–4] and of an experimental nature.[5–17] Hertel *et al.* have reviewed the subject in depth.[18] Our own work[19–22] concerns the short-lived Ne** $\{(2p)^5(3p)\}$ atoms.

Experiments with ground-state and metastable atoms pose considerably fewer experimental problems than similar experiments with short-lived atoms. For the latter cross sections are usually smaller. More significant, though, are the low effective particle densities associated with short lifetimes. This does not apply to atoms in a short-lived level that on excitation with a laser constitutes a two-level system with the metastable level from which it is produced. Hence the relative abundance of experiments with two-level systems. As an expedient solution to the low-density problem, bulk experiments have enjoyed considerable favor. Their large sensitivity, however, necessarily implies a low resolution. In a study of cross-section polarization effects and energy dependence, a crossed-beam experiment is much to be preferred. The relative velocity of the collision partners is well defined, both as to orientation and as to magnitude. The energy range is much larger, as well. In spite of these obvious advantages, experiments of this type have been reported only recently.[6,7]

We have constructed a novel crossed-beam apparatus that makes possible a variety of experiments with short-lived (neon) atoms that are not part of a two-level system. To a significant extent, it can be said to combine the high resolution of crossed-beam experiment with the high sensitivity of bulk experiments.

In the short-lived atoms under discussion (be they the rather simple one-electron alkali–metal[4–6,12–14] and two-electron alkaline–earth[3,7–9,15] systems or, as in the present paper, noble gas atoms) the examination of polarization effects, in particular, is worthwhile. The outer electron occupies a relatively outlying (np) orbital. This, as opposed to the closer (ns) orbital of the corresponding metastable atoms. With an electron so far out, the initial orientation of the electronic angular momentum with respect to the asymptotic relative velocity of the collision partners may be expected to have a correspondingly large effect on the outcome of the collision process. The core hole in noble gas atoms has less direct influence on the potential surfaces. However, its orientation, which of course is coupled to that of the valence electron, will be of importance in a process like Penning ionization where the empty core orbital plays an active role.

 0021-9606/88/204777-22$02.10

From polarization effects many interesting features of the potential surfaces and collision dynamics of the systems in question can be deduced. It is possible to prepare the short-lived atoms in a well-defined asymptotic orientation by use of a polarized laser.

The crossed-beam experiment which is the subject of this paper is concerned with the study of the inelastic intramultiplet mixing process

$$\mathrm{Ne}^{**}\{(2p)^5(3p)\}_k + \mathrm{X} \rightarrow \mathrm{Ne}^{**}\{(2p)^5(3p)\}_l + \mathrm{X}. \quad (1)$$

Here X may in principle be any atom/molecule in the electronic ground state. So far, for reasons explained in Ref. 20, the Ne**–He system has received most attention. The Ne** $\{(2p)^5(3p)\}_k \equiv \{\alpha\}_k$ states, with k running from 1 to 10 with decreasing energy (as in the Paschen notation), are shown in Fig. 1. Their lifetimes are on the order of $\tau \simeq 20$ ns. The total energy spread of the multiplet is $\Delta E_{1,10} = 584$ meV. Also shown in the figure is the Ne*$\{(2p)^5(3s)\}_i$ multiplet, of which the Ne*($^3P_0$) and Ne*($^3P_2$) states are metastable. Excitation by laser from these to one of the short-lived Ne** states occurs at wavelengths $\lambda_{ik} \simeq 600$–700 nm. Radiative decay from the short-lived states is in the same visible wavelength region. The Ne*($^3P_2$) and Ne**$\{\alpha\}_9$ states form a two-level system at $\lambda_{ik} = 640.2$ nm.

While the present paper will go into substantially more detail, a general overview of the corssed-beam experiment has been given already in Ref. 20. Both here and in Ref. 21 absolute polarized-atom Ne**–He cross sections $Q^{|M_k|}_{l \leftarrow k}$ have been presented for a number of $\{\alpha\}_k \rightarrow \{\alpha\}_l$ transitions at thermal energies. Here M_k is the magnetic quantum number of the electronic angular momentum **J** of the initial $\{\alpha\}_k$ state along the asymptotic relative velocity **g**, i.e., the z-axis. Cross-section data for the Ne**–Ne system are given in Ref. 22. Large polarization effects have been observed, as well as considerable variation in cross-section magnitude.

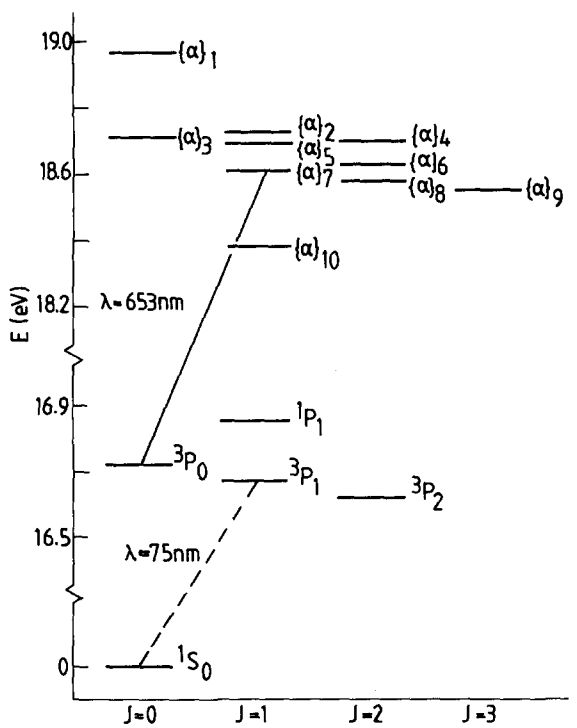

FIG. 1. Energy-level diagram of the Ne*$\{(2p)^5(3s)\}$ (Russell–Saunders notation) and Ne**$\{(2p)^5(3p)\}$ (Paschen numbering) excited states, grouped by their electronic angular momentum quantum number J.

From a theoretical point of view, in our analysis of the experimental results we have made use of the Ne**–He model potentials of Hennecart[1,11] and Masnou-Seeuws.[1] As accurate information on coupling potentials is indispensible for an explanation of polarization effects, their availability is very fortunate. Reference 20 describes our fully quantum-mechanical coupled-channels calculations on the Ne**–He inelastic scattering problem, which use the above potentials as input. The Ne**–Ne problem, which is complicated by the presence of additional symmetries not present for Ne**–He, is discussed in Ref. 22. At the present thermal energies these coupled-channels calculations (requiring several hours on a Burroughs B7900 mainframe computer for each energy value) yield cross sections that generally agree well with the experimental results.[20,21] Regrettably, however, this constitutes basically a "black box" approach, in that the link between input (model potentials) and output (cross sections) is rather remote. This problem is addressed in Ref. 21, which offers a semiclassical analysis of transitions between states in the $\{\alpha\}_{k=4,5,6,7}$ group. The presence of several avoided crossings between their adiabatic potentials, with its implication of strong localized radial coupling, both emphasizes the group's relatively isolated position within the larger Ne** multiplet and suggests the relevancy of a description in semiclassical terms. The semiclassical calculations turn out to provide superior insight in the Ne**–He interaction and collision dynamics.

In this paper, we describe the design, operation and calibration of a crossed-beam experiment for the study of total cross sections for the Ne** + X intramultiplet mixing process of Eq. (1). We start out, in Sec. II, by considering the signals expected from this kind of experiment. This inevitably leads to a number of experimental requirements, that have heavily influenced the design of the apparatus. In Sec. III, the ultimate experimental setup is described, first in general terms, then in more detail. There follows Sec. IV on the calibration of the experiment, i.e., the way in which physically meaningful results may be obtained and subsequently analyzed. Section V deals first with data analysis in general and then with the various experiments it is possible to perform in the present setup. Examples are given of each. Lastly, some concluding remarks are given in Sec. VI. All in all, we aim to provide as complete an overview of the experiment as possible.

II. EXPERIMENTAL SIGNALS AND DESIGN CONSIDERATIONS

The design of a crossed-beam experiment for the investigation of inelastic collision processes with short-lived electronically excited atoms has to be considered very carefully. The more so when the reaction products can only be detected through their radiative decay. Let us assume a configuration of three crossing beams: the primary beam of metastable Ne* atoms, the laser beam tuned to a Ne* → Ne** transition, and

the secondary beam of electronic ground-state particles X. The experiment can be summed up in the reaction equation

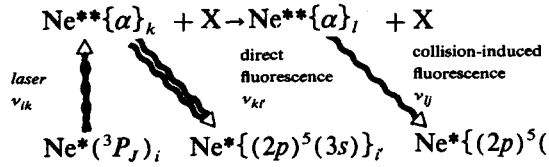

(2)

Through optical pumping the metastable $Ne^*(^3P_J)_i$ atoms are excited to the initial short-lived $Ne^{**}\{\alpha\}_k$ state. Nearly all of the $\{\alpha\}_k$ atoms will be deexcited by spontaneous emission of what is to be called "direct" fluorescence radiation. With the secondary beam passing through the intersection of primary and laser beam, however, a small fraction of the $\{\alpha\}_k$ atoms will undergo an inelastic collision. This gives rise to population of the $Ne^{**}\{\alpha\}_l$ state, among others. This state, too, exhibits spontaneous decay within its natural lifetime $\tau \simeq 20$ ns, generating "collision-induced" fluorescence radiation. The latter usually comprises several frequencies, like the direct fluorescence. By measuring a single line of both types of fluorescence, we obtain a measure for the number of atoms in the k and l states, respectively, and thus ultimately for the $\{\alpha\}_k \rightarrow \{\alpha\}_l$ cross section. The major experimental problems encountered follow directly from the expressions for the count rates I_k (s^{-1}) for the direct fluorescence from the initial state $\{\alpha\}_k$, and I_l (s^{-1}) for the collision-induced fluorescence from the final state $\{\alpha\}_l$. These are given by

$$I_k = \eta_k \dot{N}_k R_k, \tag{3a}$$

$$I_l = \eta_l \dot{N}_k R_k \frac{g}{v_1} n_2 l_\tau Q_{l \leftarrow k} \tag{3b}$$

with η_k and η_l the photon detection efficiency for the direct and collision-induced fluorescence, $\dot{N}_k$ (s^{-1}) the flow of initial state particles through the scattering volume, v_1 the primary-beam velocity, g the relative velocity of the collision partners, n_2 the secondary-beam density, $l_\tau = v_1 \tau_k = v_1 / A_k$ the "lifepath" of the initial state particles, and $Q_{l \leftarrow k}$ the total inelastic cross section for the $\{\alpha\}_k \rightarrow \{\alpha\}_l$ transition. Through the recycling factor $R_k \simeq 1/(1 - A_{ki}/A_k)$ we take into account that a fraction A_{ki}/A_k of the atoms in the initial short-lived $\{\alpha\}_k$ state is recycled via the metastable $Ne^*(^3P_J)$ lower level of the optical pumping transition. With appropriate laser power almost all of the $Ne^*(^3P_J)$ atoms in the primary beam are excited to the $\{\alpha\}_k$ state, resulting in $\dot{N}_k = C_J \dot{N}_{Ne^*(J)}$, with C_J the relative population for the metastable state used for the $Ne^{**}\{\alpha\}_k$ production. In Eq. (3b) for the collision-induced fluorescence signal we recognize the usual "*nlQ*" product of a crossed-beam experiment, modified by the use of the "lifepath" instead of the length of the scattering volume. Of course, Eq. (3) does not apply to the two-level $Ne^*(^3P_2)$–$Ne^{**}\{\alpha\}_9$ system. Here the Ne atom oscillates between the metastable and short-lived levels all through the scattering volume, with much larger signals as a result.

Strictly speaking, on its way to the scattering center the primary beam will be attenuated by secondary-beam particles; if not in the secondary beam itself, then in the form of residual gas. This implies that the $\dot{N}_k$ of Eq. (3) are related to the output of the primary-beam source through a transmission factor T_k, with

$$T_k = \dot{N}_k / \dot{N}_k(-\infty). \tag{4}$$

The importance of this phenomenon will become apparent soon; for the moment we will disregard it.

From Eq. (3) we can deduce the practical problems which our particular experiment presents. Both the lifepath l_τ of the short-lived atoms and the transition cross section $Q_{l \leftarrow k}$ are very small: $l_\tau \simeq 20\ \mu$m, $Q_{l \leftarrow k} \simeq 1$ Å^2. This implies that considerable effort will be required to obtain a measurable collision-induced fluorescence signal, i.e., a signal that can be separated from the inevitable background. First, we must maximize primary-beam flow $\dot{N}_{Ne^*}$ and secondary beam density n_2. Second, extremely efficient detection of fluorescence photons is needed, that is to say large values of the optical detection efficiency η_l. As to background radiation, from Eqs. (3a) and (3b) it follows that at all times the direct fluorescence radiation will be several orders of magnitude larger than the collision-induced fluorescence. This calls for almost complete suppression of the former. Of course, the same holds for other sources of background radiation.

Because both factors R_k and g/v_1 in Eq. (3b) are on the order of unity, the product of remaining factors must measure

$$\eta_l \dot{N}_k n_2 \gtrsim 5 \times 10^{27} \text{m}^{-3}\,\text{s}^{-1} \tag{5}$$

to obtain a count rate $I_l \gtrsim 10^3 \text{s}^{-1}$, for l_τ and $Q_{l \leftarrow k}$ as given above. In a nonoptimized, standard crossed-beam experiment,[23] we find typical values $\eta_l \simeq 10^{-4}$, $n_2 \simeq 5 \times 10^{17}$ m^{-3}, and $\dot{N}_k = 10^8$ s^{-1} (for a primary-beam center-line intensity of 10^{14} s^{-1} sr^{-1} and 10^{-6} sr^{-1} solid angle). This results in

$$\eta_l \dot{N}_k n_2 \simeq 5 \times 10^{21} \text{m}^{-3}\,\text{s}^{-1} \tag{6}$$

and a completely impractical count rate of $I_l \simeq 10^{-3}$ s^{-1}!

III. EXPERIMENTAL SETUP

A. Overview

The special requirements of the present experiment have led us to design a novel crossed-beam apparatus, of which a schematic view is given in Fig. 2. Figure 3 offers a more general overview of the experimental setup.

The primary beam of metastable Ne* atoms originates in a discharge-excited supersonic expansion, or thermal metastable source (TMS).[24] The source chamber, pumped by a 110 ℓ/s turbomolecular pump, is connected by a 0.5 mm ϕ skimmer to the main vacuum chamber. The latter was machined from a solid block of aluminum. It is pumped by an oil-diffusion pump with an effective pumping speed of 1200 ℓ/s, for a pressure, with no secondary beam, of $p \simeq 2 \times 10^{-7}$ Torr. The maximum center-line $Ne^*(^3P_2)$ intensity for the TMS, operated with pure neon, is about $j_{i,0} \simeq 10^{14}$ s^{-1} sr^{-1}; the $Ne^*(^3P_2) : Ne^*(^3P_0)$ ratio is roughly statistical, i.e., 5 : 1. Downstream of the skimmer, all charged particles are removed by condenser plates. The required high density of metastable Ne* atoms in the collision region is obtained by virtue of its small distance to the TMS. With the collision region situated about 90 mm from the

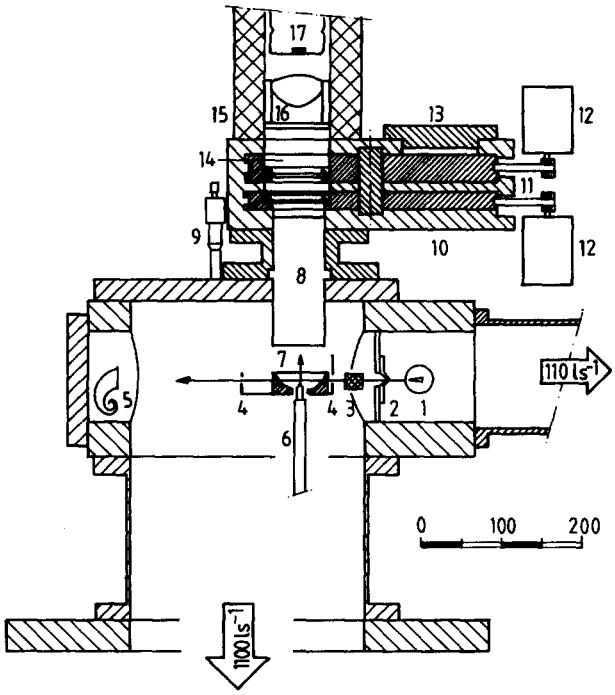

FIG. 2. Schematic drawing of the crossed-beam apparatus. The scale is in mm. To improve visibility, the size of, e.g., diaphragm and mirror openings has been exaggerated. (1) Primary beam source; (2) skimmer; (3) condenser plates; (4) primary-beam diaphragms; (5) primary-beam light trap; (6) vertically adjustable secondary-beam nozzle; (7) parabolic mirror; (8) plexiglass light guide; (9) micrometer for nozzle adjustment; (10) filter assembly; (11) belt-driven rotatable filter disks; (12) stepper motors; (13) filter loading gate; (14) interference and cutoff filters in filter holders; (15) cooled photomultiplier housing; (16) no-dew aspherical lens assembly; (17) photomultiplier.

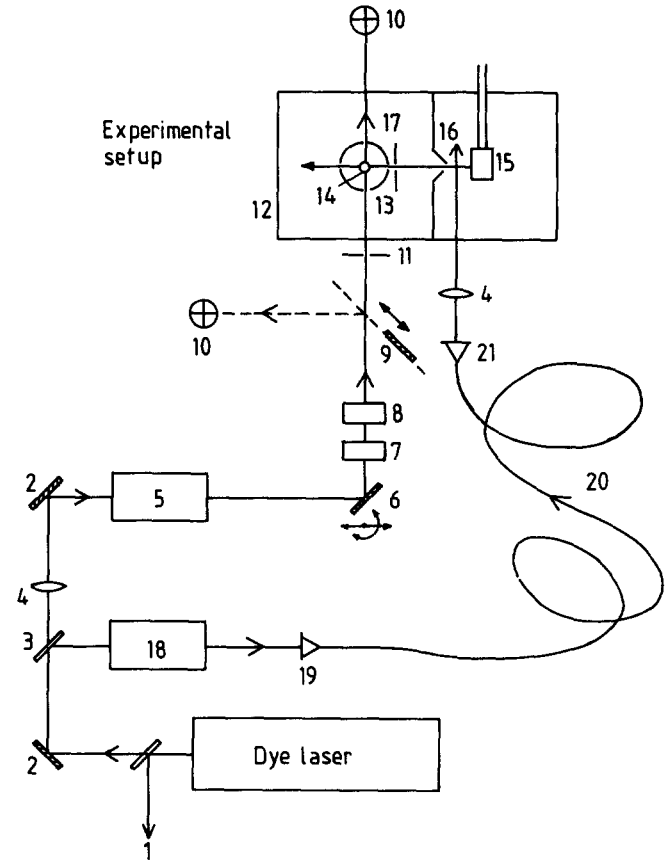

FIG. 3. Overview of the experimental setup. A separate atomic-beam setup controls the laser-frequency stabilization. (1) To laser-frequency stabilization setup; (2) mirror; (3) beam splitter; (4) lens; (5) laser-power stabilization; (6) rotatable/translatable mirror; (7) rotatable planparallel plate; (8) laser polarization rotator; (9) movable mirror; (10) quadrant detector; (11) diaphragm; (12) vacuum chamber; (13) parabolic mirror; (14) secondary-beam nozzle; (15) primary-beam source; (16) skimmer; (17) primary-beam diaphragm; (18) laser chopper; (19) optical-fiber entrance; (20) optical fiber; (21) optical-fiber exit.

TMS, the primary-beam density is $n_{Ne^*} \simeq 10^{13}$ m^{-3}. Metastable particle flow $\dot{N}_{Ne^*}$ through the collision region is determined by the 1 mm ϕ primary-beam defining diaphragm at 60 mm from the skimmer. This geometry results in $\dot{N}_{Ne^*} \simeq 2\times 10^{10}$ s^{-1}. A 2 mm ϕ diaphragm downstream of the collision region is used for primary-beam alignment. Still further on, a light trap collects the light from the TMS.

The secondary beam is formed by a skimmerless supersonic expansion (nozzle diameter $2R_n = 50$ μm). This allows a very small distance from the nozzle to the collision region and a correspondingly high secondary-beam density. In our apparatus the distance may be adjusted from 0 to 12 mm by a micrometer outside the vacuum chamber, through a pin-lever construction. Typically, the distance is 2 mm. For noble gas atoms at a reservoir pressure $p_{2,0} = 120$ Torr and temperature $T_2 = 300$ K, the secondary-beam density is then given by both theory and experiment[25] as $n_2 \simeq 3\times 10^{20}$ m^{-3}. Secondary-beam gas flow is controlled by two pneumatic valves. Upon closure with one valve of the gas supply, the other valve allows pumping of the gas leads. From a working pressure of about 4×10^{-6} Torr, it takes about 10 s for the pressure to be restored to 2×10^{-7} Torr. Depending on the secondary-beam gas, a longer waiting period may be necessary. In summary, we have fulfilled the first experimental requirement of high primary- and secondary-beam densities by situating both primary- and secondary-beam sources as close to the collision region as possible.

The laser beam, linearly polarized, from a Spectra Physics 580A cw single mode dye laser system crosses the primary beam of metastable Ne* atoms at right angles. The required 590–660 nm range is covered by the easy-to-use rhodamine 6G, rhodamine 6B, and DCM dyes. The laser frequency is stabilized to within 0.5 MHz rms deviation of the transition frequency ν_{ik}.[26] In addition, the frequency is continuously tunable under computer control within a range of $\nu_{ik} \pm 200$ MHz, in steps as small as 0.1 MHz. Laser power (typically maintained at $P \lesssim 0.2$ mW in the collision region) is controlled and stabilized ($\pm 2\%$) with an electro-optical modulator. Two lenses ($f_1 = 500$ mm, $f_2 = 2000$ mm) are used to obtain a waist in the collision region ($1/e^2$ radius $W \simeq 0.4$ mm). The laser polarization can be rotated by means of a stepper-motor driven $\lambda/2$ plate.

Because of the short lifetimes of the Ne**$\{\alpha\}_k$ atoms produced in the optical pumping process, it is the laser beam that determines the lateral position of the collision region. The secondary beam has to pass through the crossing point of the laser and primary beams. In view of the vital importance of proper laser-beam alignment, two quadrant diodes defining the laser-beam axis have been incorporated in the

setup. Alignment itself is effected, in the horizontal plane containing the primary-beam axis, by means of a stepper-motor driven rotatable and translatable mirror. For vertical movement of the laser beam we use a rotatable planparallel plate, stepper-motor actuated as well.

The dependence of the optical pumping process on the presence of low-strength magnetic fields[27] has necessitated surrounding the vacuum chamber with a set of six rectangular Helmholtz-like coils. With these any field $B \lesssim 2$ G in the scattering center can be nullified, the Earth's field ($B \lesssim 0.5$ G) in particular.

In order to perform time-of-flight measurements, part of the laser beam from the dye laser may be branched off with a beam splitter. This second beam is directed through a fiber to the primary beam, between the nozzle of the TMS and the skimmer. An electro-optical modulator in combination with a polarizer allows rapid switching on and off of the laser beam. With the laser attuned to a $\mathrm{Ne}^*(^3P_{0,2}) \rightarrow \mathrm{Ne}^{**}\{\alpha\}_k$ transition, the Ne* density in the primary beam will then be modulated accordingly. A laser power of $P \simeq 0.5$ mW suffices for nearly 100% modulation of the primary beam.

The optical detection system uses a parabolic mirror for the collection of fluorescence radiation, and narrow-band interference filters for wavelength selection. Additional suppression of background light is achieved through cutoff filters. All filters are housed in a separate filter assembly. The transmitted photons are focused on the cathode of a photomultiplier. For a more detailed discussion of the optical system, we refer to the next section. Ultimately, a high detection efficiency is achieved: typically, $\eta_l \simeq 10^{-3}$ per photon produced in the collision region. Like the primary-beam defining diaphragms, the secondary–beam nozzle, and the quadrant diodes used for laser-beam alignment, the parabolic mirror has been rigidly attached to the top flange of the vacuum chamber. The latter can therefore be removed without compromising the alignment of these components. The vital performance characteristics of the crossed-beam apparatus have been summarized in Table I. A look at the $\eta_l \dot{N}_k n_2$ product shows that the tentative requirement of Eq. (5) has been all but satisfied. The overall figure of merit in the thermal energy range is about 1 kHz/Å^2, for the number of counts per unit of inelastic cross section. The background count rate ranges from 2 to 15 kHz and is due mainly to the line emission from the discharge in the TMS.

TABLE I. Performance characteristics of the crossed-beam apparatus. The symbols have been defined in the text. The value of the "performance number" is to be compared with that given in Eq. (5)

Name	Quantity	Typical value
Optical detection efficiency	η_l (counts/photon)	1×10^{-3}
Primary-beam flux	$\dot{N}_{\mathrm{Ne}^*}$ (s^{-1})	2×10^{10}
Primary-beam transmission	T_k	0.35
Optical pumping recycling factor	R_k	1.5
Lab–c.m. conversion	g/v_1	$\simeq 1$
Secondary-beam density	n_2 (m^{-3})	3×10^{20}
Lifepath	l_τ (m)	2×10^{-5}
Inelastic cross section	$Q_{l\leftarrow k}$ (m^2)	1×10^{-20}
Performance number	$\eta_l \dot{N}_k n_2$ (m^{-3} s^{-1})	3×10^{27}
Count rate	I_l (s^{-1})	0.63×10^3

B. Optical detection system

The demands made on the optical detection system, i.e., a large detection efficiency η and effective suppression of background radiation, have been met by employing narrow-band interference filters for wavelength selection. As the interference filters require perpendicular incidence, the collision region is situated near the focal point of a parabolic mirror. Thus a substantial portion of the fluorescence radiation is imaged into a (nearly) parallel beam. Solid-angle efficiency of the parabolic mirror is approximately 0.40, i.e., a solid angle of 1.6 π is collected. The condition of (nearly) perpendicular incidence on the interference filters poses no serious limitation on the acceptance of the optical system. The optical phase volume of the parabolic mirror–interference filter combination is very much larger than can be attained with a monochromator. Originally, a Melles Griot parabolic mirror ($f = 10.2$ mm) was used, with a rhodium coating on a nickel substrate. Entrance and exit ports for the primary and laser beams have been added. An opening in the bottom for the secondary-beam nozzle was present already. This mirror has now been replaced by a nonmagnetic all-aluminum specimen of the same specifications and with a comparable reflection coefficient $R \simeq 0.80$. To interchange filters during the experiment, they have been positioned outside the vacuum chamber. To minimize the loss due to divergence of the light from the parabolic mirror, a plexiglass cylinder has been used as a transparent vacuum seal. This acts as a light guide, on account of complete internal reflection.

The interference filters [peak transmission $T_{\max} \simeq 0.70$, 2 nm full width at half-maximum (FWHM), 10 nm FW at 10^{-6} transmission] (see Fig. 12 in the next section) allow us to monitor a single line of either the collision-induced fluorescence from the final state $\{\alpha\}_l$, or the direct fluorescence from the initial state $\{\alpha\}_k$. Generally, we have ample background suppression. In some cases the wavelength spacing to a nearby direct fluorescence line is simply too small. Where necessary, additional suppression of background light is achieved by the use of colored glass cutoff filters. When measuring direct fluorescence radiation, neutral density filters are added to the optical system in order to guarantee a linear response of the counting system.

Given the important role that filters (interference filters in particular) play in the experiment, a special filter assembly has been designed, that combines easy interchangeability of the filters with hermetic optical sealing. It is shown in Fig. 4. The two flat disks, which are its major constituents, have five filter chambers each. The lower and upper disks accomodate one and two filters per chamber, respectively. For this purpose, the filters have all been mounted in standard filter holders. The disks may be rotated independently, so as to bring any combination of the 2×5 filter positions into the light path of the optical system. The filters may be rearranged in the disks through a cover in the assembly, diagonally opposite the photomultiplier housing. One filter position in the upper disk has been sacrificed to give access to the

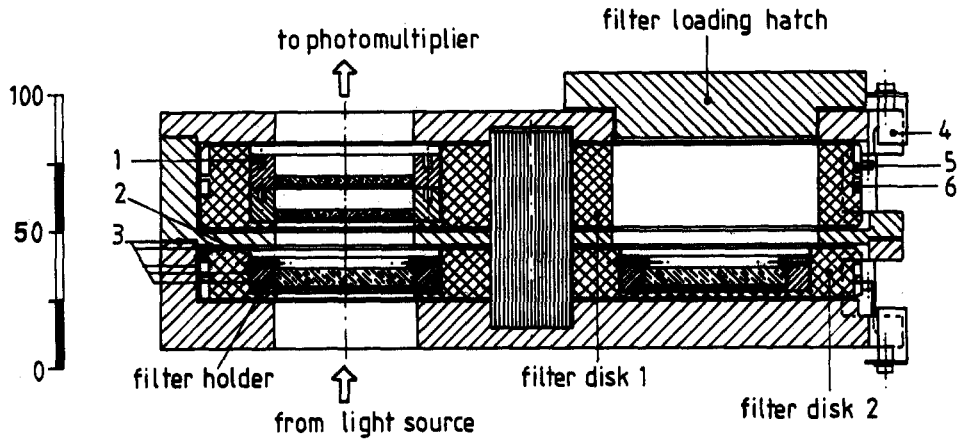

FIG. 4. Schematic drawing of the filter assembly. Its major components have been indicated. The scale is in mm. The thickness of the fabric sealing between the parts has been exaggerated. (1) Threaded hole for filter-holder removal; (2) lock-screw securing interference filter; (3) fabric sealing between moving and nonmoving parts; (4) microswitch (one of four per filter disk); (5) activating notch for microswitch; (6) groove for belt driving filter disk.

filters in the lower disk. Through the use of various fabrics, sandwiched between moving and nonmoving parts, it has been ensured that no light from the surroundings can penetrate into the optical system. Likewise, heavily compressed fabric sealing between both filters and filter holders and filter holders and filter chambers prevents light from the experiment from circumventing the filters. With a metal disk replacing the filters in front of the photomultiplier, no rise in the dark-count number of the photomultiplier (about 12 s^{-1}) is observed under any circumstances.

The filter disks can be rotated by hand. However, the experiment requires the filters in front of the photomultiplier to be changed at short time intervals. Therefore, a pair of stepper motors has been mounted, each driving a disk through a belt around its circumference. These stepper motors are under computer control. The computer checks for proper positioning of the disks by reading out an array of four microswitches, actuated by notches cut into each disk. One of the notches serves for indexing purposes only, the other three are needed to unambiguously identify each of the five filter positions per disk. Of course, at all times the direction of rotation is chosen so as to minimize the number of steps to the next filter position. Through parallel processes in the experiment computer, the disks are made to rotate simultaneously. Lastly, lest during the filter change the photomultiplier is unintentionally exposed to excessive light intensity, the laser beam is interrupted by a computer-actuated shutter.

After passing through the filters, the photons are focused by an aspherical lense ($f = 39$ mm) onto the 9 mm ϕ cathode of a selected red-sensitive EMI 9862 S20 photomultiplier in a housing cooled to -20 °C. Quantum efficiency of the photomultiplier is a low 3%–5%, depending on the wavelength. Finally, pulses from the photomultiplier are converted into TTL pulses by an EG&G PARC model 1182 amplifier/discriminator. As mentioned before, in the present configuration the overall detection efficiency of the optical system is typically $\eta_l \simeq 10^{-3}$ counts per photon produced in the collision region.

C. Laser-beam alignment

The crucial importance of proper laser-beam alignment has already been indicated and will be reexamined later. Laser-beam diameter is on the order of 1 mm ($1/e^2$ contour) and an accuracy of better than 0.05 mm in both the horizontal and the vertical position of the laser beam–primary beam intersection is required. Because of this it was found necessary to establish both a way to fix the true laser-beam axis in space, and to maneuver the laser beam into the proper position. In view of the desired accuracy and in order to minimize the time spent on alignment, an automated procedure is preferred. The heart of the alignment system are two light-sensitive quadrant diodes. As shown in Fig. 5, these are divided into four equal parts, each of which will yield a signal proportional to the amount of incoming light. From the right–left and up–down differences in signal magnitude, the position of a laser beam striking the detector can be determined. As an example, Fig. 5 shows the result of a horizontal scan of the laser beam across the detector surface. The linear behavior of the right–left signal about the origin allows a highly accurate estimate of the laser beam position.

Two quadrant diodes are needed to fix a line in space. The second of these has been situated for the laser beam to hit upon its exit from the vacuum chamber. The first has been placed at right angles to the laser beam. An angled

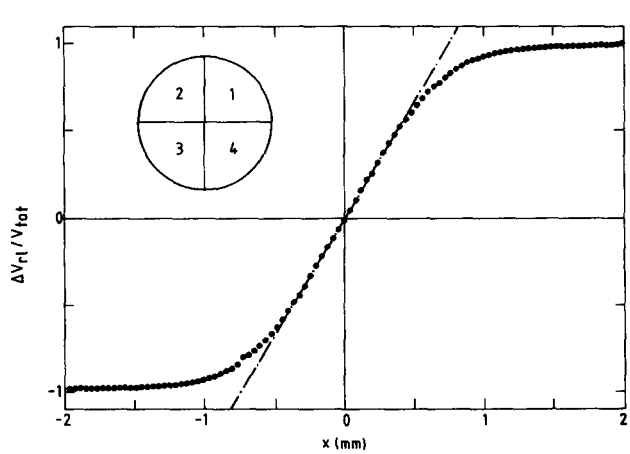

FIG. 5. The scaled differential right–left signal $\Delta V_{rl} = (V_1 + V_4) - (V_2 + V_3)$, for a 1.3 mm diameter ($1/e^2$) approximately Gaussian laser beam moving horizontally over a quadrant detector. The signal displays linear behavior about the center position. This allows positioning of the laser beam by the fast and accurate method of interpolation.

mirror moving into and out of the laser beam makes it possible to illuminate the first and second detector in turn. This setup has been pictured in Fig. 3. A linear bearing allows one-dimensional movement of the mirror only, answering all demands regarding positioning accuracy. Having the detector itself return again and again to the same position in the beam would require considerably more effort. The signals from the detectors are fed through a multiplexer to four gates of an ADC converter and read by the computer. Moving the mirror is done by stepper motor, under computer control. Both detectors and mirror are mounted on a yoke, which is fixed rigidly to the lid of the vacuum chamber. Thus their position with respect to the primary-beam-defining diaphragms and the secondary-beam nozzle is fixed, as well. Initial alignment of the detectors is done both visually and by, for instance, maximizing the direct fluorescence signal with respect to the angle between laser and primary beam. Horizontal and vertical positioning of the detector is possible in 0.01 mm increments, with a micrometer.

With the quadrant detectors in place, it remains to devise an automated alignment procedure. For this, use was made of the translator/rotator module[28] mentioned earlier, whose mirror can be translated and rotated independently by stepper motors. Thus the laser beam can be moved at will in the horizontal plane. In particular, by using both stepper motors under computer control, rotation about any given point, within limits, becomes feasible. At present translation is in 0.01 mm steps and rotation in 0.2 mrad steps, over a total range of 15 mm and 200 mrad, respectively. This is commensurate with the requirements of the experiment. In a more simple module, a stepper motor rotating a planparallel plate can move the laser beam up and down in steps of approximately 0.01 mm. There is at present no provision for rotating the laser beam in the vertical plane. This is least critical to a proper outcome of the experiment, however, and alignment by hand to within 2 mrad prior to starting the automated alignment procedure suffices.

Horizontal alignment is performed first. To begin with, the laser beam is rotated about the first detector into alignment with the second. Subsequently this is repeated the other way around, the laser beam now being aligned with the first detector, while alignment is maintained on the second detector. This procedure is iterated, if necessary. In the end, the laser beam can thus be aligned to within 0.1 mrad. This corresponds to a horizontal position error of less than 0.05 mm on the two detectors, well within their linear range (see Fig. 5). By translating the laser beam a scan can then be made over the two detectors, akin to the one in Fig. 5, though over a smaller range and in fewer steps. Since the position of the scattering center between the two detectors is known, the laser beam can in principle be made to pass within approximately 0.005 mm, while maintaining its smaller than 0.1 mrad misalignment. In the vertical direction, the alignment procedure essentially duplicates the last stage of the horizontal alignment. Now, the translation is performed by rotating the planparallel plate. The whole laser beam alignment process, apart from the initial positioning by hand which is needed only intermittently, takes the computer about 15 min.

D. Pseudo-random laser chopper

In the present minibeam setup, the metastable primary-beam atoms traverse only a short distance $L \simeq 90$ mm from the thermal metastable beam source to the collision region. Average beam velocity is about $v_1 \simeq 1000\ \mathrm{m\ s^{-1}}$. For time-of-flight (TOF) measurements to yield a properly resolved velocity spectrum with, say, $\Delta v_1/v_1 \lesssim 0.5\%$–$5\%$, channel times $t_k \lesssim 0.5 - 5\,\mu\mathrm{s}$ with correspondingly short burst times t_b are required. In addition, the low signal strengths associated with the collision-induced fluorescence in particular, indicate the use of a pseudo-random chopper function which has a much larger open time fraction than the more usual single-burst chopper function.[29] However, it is very difficult to synchronize a pseudo-random mechanical chopper with the multichannel scaler counting the signal in its time channels. Furthermore, the short burst times required rule out a mechanical chopper, for reasons of mechanical strength along.[30] This means, that an optical laser chopper presents the only viable option for TOF measurements. Of course, the limited amount of room available in our very compact apparatus also favors this technique, wherein the metastable $\mathrm{Ne}^*(^3P_{0,2})$ density in the primary beam is modulated by a laser beam attuned to a $\mathrm{Ne}^*(^3P_{0,2}) \rightarrow \mathrm{Ne}^{**}\{\alpha\}_k$ transition.

The chopper laser beam is branched off with a beam splitter from the laser beam that produces the initial short-lived $\mathrm{Ne}^{**}\{\alpha\}_k$ atoms in the scattering volume. A Coherent model 28 electro-optical crystal is used together with a fast high voltage amplifier driven by TTL pulses, to rotate the laser's polarization over 90°, and back. In combination with a polarizer, this effectively turns the beam off and on. With the laser beam directed through a fiber to the space between the nozzle of the TMS and the skimmer, the primary beam of metastable $\mathrm{Ne}^*(^3P_{0,2})$ atoms is consequently turned "on" and "off". Up to 98% modulation of the relevant Ne* flux can be achieved in this way, with a laser power $P \simeq 0.5$ mW.

The fast multiscaler[31] has 255 time channels, with a minimum channel time $t_k = 500$ ns. It is able to store a preprogrammed pseudo-random or single-burst series in its memory. This may be administered in the form of TTL pulses to the high voltage amplifier controlling the electro-optical modulator. The fluorescence signals from the collision volume are accumulated in the multiscaler's time channels. This arrangement ensures the proper synchronization of chopper and multiscaler. Channel times t_k are derived from an external 20 MHz clock. It is possible to select burst times $t_b = i/5 * t_k$, with $i = 1,...,5$.

The multiscaler was designed to function as an intelligent interface in a computer-controlled measuring system. Prior to measuring, the computer loads the desired pseudo-random or single-burst series of an arbitrary length $N \leqslant 255$ into the multiscaler's memory. Then, after a starting signal from the computer, the multiscaler accumulates data in its time channels for a maximum of 65 000 chopper periods. Overflow errors and the like are reported back to the computer. In the meantime, the computer is free to perform other tasks, such as checking the status of the experiment or performing a calculation upon the data already collected.

After its final period, the multiscaler notifies the computer which samples the accumulated data and restarts the cycle.

E. Computer control

The complexity and required accuracy of the experiment are such, that it could hardly be run without the aid of a computer. This applies both to the actual measuring process and to the data gathering and analysis. As will be detailed in Sec. IV, every basic cross-section measurement requires the frequent tuning and detuning of the laser, the rotation of filters for direct and collision-induced fluorescence, and the turning on and off of the secondary beam. A complete cross-section measurement (Sec. V) requires that, e.g., the laser polarization be rotated, or the laser beam moved, or the secondary-beam gas changed. With the exception, at present, of the latter, all of the above can be performed by computer. So can, as we have seen already, the alignment of the laser beam.

The experiment computer was developed in the Physics Department on the basis of the Motorola M68000 microprocessor.[32] It is programmed in the Pascal-related language PEP (Program Editor and Processor),[33] which is an interpreter-based language and thus especially suited to an experimental environment. The computer's capacity to handle several parallel processes at a time is also very useful in this respect. Experiment-control and data-gathering procedures are collected in libraries in the microcomputer's memory (1 Mbyte, at present) and are accessed by the measuring program.

The computer's connection to the experimental setup is through the modular Eurobus interface system.[34] A number of interfaces is available. For data gathering, multiple channel ADC's, scalers and preset scalers are used (the latter two combine with a 20 MHz clock into a frequency counter). The multiscaler mentioned above also adheres to the Eurobus protocol. Basic functions of the experimental setup (associated with stepper motors, microswitches, relays, etc.) are handled by stepper-motor interfaces, input/output registers, and DAC's. The input/output register also provides a hardware-based communication's link with the separate LSI 11/02 microcomputer controlling the laser system. In addition information is exchanged through a common file on background memory.

Both experiment and laser computer are connected, through the departmental network Budgetnet,[35] to a central MicroVax II computer, which acts as host in a file-server capacity. After preliminary analysis, data gathered by the experiment computer are sent to the host computer, along Budgetnet's 2.5 Mbaud serial line. From the host, data can be sent to the computing center's Burroughs B7900 mainframe computer over the university's 9600 baud TUE network, for further analysis. Once the group's network of PC/AT compatible microcomputers has been connected to Budgetnet, these will largely supersede the B7900 as a tool for full data analysis.

IV. CALIBRATION OF THE EXPERIMENT

A. Measuring routine

Our aim is to determine the collision-induced and direct fluorescence signals I_l and I_k, as defined in Eq. (3). Ideally, this would involve two measurements only, with different interference filters. In practice, however, we will have to correct for background light which cannot be entirely suppressed by the optical system. The main sources of background are light from the surroundings, stray light from the laser, direct fluorescence from the initial $Ne^{**}\{\alpha\}_k$ level, and stray light from the primary-beam source (TMS). While with some effort the first two may be reduced to an extent that the interference filters are capable of suppressing them almost entirely, this does not hold for the other two. Of course, light from the TMS contains the very wavelengths that we are investigating. For the relative importance of the various sources of background in our apparatus, see Table II.

In order to correct for background contributions, two further diagnostics are employed in addition to the use of different filters for direct and collision-induced fluorescence. The first of these is modulation of the optical pumping process by which the initial $Ne^{**}\{\alpha\}_k$ atoms are produced. Rather than simply turning the laser "on" and "off," which allows for no easy correction for stray laser light, the laser is tuned and detuned sufficiently (about 100 MHz) to preclude excitation of the metastable $Ne^*(^3P_{0,2})$ atoms. The slight accompanying wavelength change makes no difference to the optical system. The second additional diagnostic is modulation of the secondary beam, by simply turning it on and off. Of course this also influences the attenuation of the primary beam by secondary-beam particles. By combining these three modulation techniques, we can devise a tactic to eliminate all background contributions.

Table III lists all possible diagnostic combinations together with the corresponding experimental signals. These consist of varying contributions from the direct fluorescence from the initial level, the collision-induced fluorescence from the final level, and background light. The "net" direct and collision-induced fluorescence signals I_l and I_k of Eq. (3) have been emphasized. The transmission factor T_k has been defined in Eq. (4). The factors $\mathcal{R}_k$ and $\mathcal{R}_l$ formally take into account the effects on the background signal B of Rayleigh scattering of background light by the high-intensity secondary beam. We also nominally allow for imperfect detuning of the laser, whereby a fraction $\epsilon > 0$ of the metastable atoms will still be pumped. Lastly, a superscript l/k used in connection with the detection efficiency $\eta_{k/l}$ indicates a

TABLE II. Typical background signals for the crossed-beam apparatus.

Background source	Signal without interference filter (s^{-1})	Signal with interference filter[a] (s^{-1})
PM dark count	12	12
Surroundings[b]	40×10^3	55
Laser[c]	50×10^6 [d]	200
TMS	30×10^3	1000
Direct fluorescence[e]	···	4000

[a] 703 nm.
[b] Normal lighting.
[c] 0.1 mW, 633 nm.
[d] Extrapolated value.
[e] 633, 650, 717 nm.

TABLE III. The settings used for signal diagnostics, and the corresponding experimental signals. See the text for explanation.

Filters for	Secondary beam	Laser beam	Signal	= Collision-induced fluorescence	+ Direct fluorescence	+ Background	"Real" signal
Collision-induced fluorescence from $\{\alpha\}_l$ level (L)	on	ν_0	$L^{on}(\nu_0)$	$= T_k\dot{N}_l\eta_l$	$+ T_k\dot{N}_k\eta_l^k$	$+ \mathscr{R}_l B_l$	$L^{on} = L^{on}(\nu_0) - L^{on}(\nu_0+\Delta\nu)$
		$\nu_0+\Delta\nu$	$L^{on}(\nu_0+\Delta\nu)$	$= \epsilon\{\ldots\ldots\}$		$+ \mathscr{R}_l B_l$	
	off	ν_0	$L^{off}(\nu_0)$	$=$	$\dot{N}_k\eta_l^k$	$+ B_l$	$L^{off} = L^{off}(\nu_0) - L^{off}(\nu_0+\Delta\nu)$
		$\nu_0+\Delta\nu$	$L^{off}(\nu_0+\Delta\nu)$	$=$	$\epsilon\{\ldots\}$	$+ B_l$	
Direct fluorescence from $\{\alpha\}_k$ level (K)	on	ν_0	$K^{on}(\nu_0)$	$= T_k\dot{N}_l\eta_k^l$	$+ T_k\dot{N}_k\eta_k$	$+ \mathscr{R}_k B_k$	$K^{on} = K^{on}(\nu_0) - K^{on}(\nu_0+\Delta\nu)$
		$\nu_0+\Delta\nu$	$K^{on}(\nu_0+\Delta\nu)$	$= \epsilon\{\ldots\ldots\}$		$+ \mathscr{R}_k B_k$	
	off	ν_0	$K^{off}(\nu_0)$	$=$	$\dot{N}_k\eta_k$	$+ B_k$	$K^{off} = K^{off}(\nu_0) - K^{off}(\nu_0+\Delta\nu)$
		$\nu_0+\Delta\nu$	$K^{off}(\nu_0+\Delta\nu)$	$=$	$\epsilon\{\ldots\}$	$+ B_k$	

radiation wavelength $\lambda_{l/k}$ at odds with the normal transmission wavelength $\lambda_{k/l}$ of the filter combination in question.

It is evident, that the additional measurements with detuned laser allow us to correct for background contributions other than those from the direct fluorescence radiation. Hence, the phrase "real" signals in Table III. In the shorthand notation of this table, we have for the averaged transmission factor T_k of Eq. (4):

$$T_k = \frac{K^{on}}{K^{off}}, \tag{7}$$

where the collision-induced contribution to the K^{on} signal has been neglected. The ratio I_l/I_k of collision-induced and directed fluorescence signals, from which the total cross section $Q_{l\leftarrow k}$ may ultimately be determined, follows from

$$\frac{I_l}{I_k} = \frac{L^{on}}{K^{on}} - \frac{L^{off}}{K^{off}}. \tag{8}$$

The second term corrects for the "leakage" of direct fluorescence radiation through the filters meant for collision-induced fluorescence. If there were no such leakage, we would of course have $L^{off} = 0$ (no secondary beam, therefore no inelastic process).

In practice, tuning and detuning of the laser (by piezoelement), turning the secondary beam on and off (by pneumatic valves), and exchanging the filters for direct and collision-induced fluorescence (by stepper motors) are under computer control. Thus, the whole sequence can easily be incorporated into the measuring program and be executed automatically. Composite time for the set of eight measurements, needed to determine a single transition cross section $Q_{l\leftarrow k}$, is generally 10–40 min, depending on cross-section magnitude. Typical signals are given in Table IV. These apply to the $\{\alpha\}_7 \rightarrow \{\alpha\}_5$ transition with asymptotic orientation $|M_5| = 0$.

From Eq. (3), the ratio I_l/I_k of collision-induced and direct fluorescence signals follows as

$$\left(\frac{I_l}{I_k}\right)_{ideal} = \frac{\eta_l}{\eta_k}\frac{g}{v_1} n_2 l_\tau Q_{l\leftarrow k}(g). \tag{9}$$

In anything other than the ideal case of a vanishing scattering volume, combining Eq. (9) with the experimental ratio I_l/I_k of Eq. (8) yields an averaged cross section value $Q_{l\leftarrow k}$. Taking the convolution effects due to a finite scattering volume V into consideration, we have in more specific terms than offered by Eq. (9):

$$\frac{I_l}{I_k} = \frac{\int_V \eta_l(\mathbf{r}) T_k(\mathbf{r}) n_k(\mathbf{r}) n_2(\mathbf{r}) g(\mathbf{r}) Q_{l\leftarrow k}(g) d\mathbf{r}}{A_k \int_V \eta_k(\mathbf{r}) T_k(\mathbf{r}) n_k(\mathbf{r}) d\mathbf{r}}. \tag{10}$$

The optical detection efficiencies η_l and η_k have been mentioned already in connection with Eq. (3), as have the primary-beam transmission factor T_k, the secondary-beam density n_2, and of course, the inelastic transition cross section $Q_{l\leftarrow k}$. Equation (10) now also takes explicit account of the density profile n_k of the initial short-lived Ne**$\{\alpha\}_k$ atoms. The Einstein coefficient $A_k = \tau_k^{-1}$ of spontaneous emission links the number of $\{\alpha\}_k$ atoms with the number $\dot{N}_k$ of photons produced, in Eq. (3). We recall, that the lifepath l_τ is given by $l_\tau = v_1\tau_k$. The small size of the scattering volume V, as determined by the density profile $n_k(\mathbf{r})$, ensures that Eq. (9) is indeed a fair approximation of Eq. (10).

In the experiment we have no detailed knowledge of primary-beam densities and therefore of absolute values n_k. However, since we are concerned only with the ratio I_l/I_k, this does not preclude the possibility of obtaining absolute cross-section values. With equal force, this applies to the optical detection efficiencies η_l and η_k, absolute values for

TABLE IV. Typical signal count rates and measuring times. These apply to the $\{\alpha\}_7 \rightarrow \{\alpha\}_5$ transition for $|M_7| = 0$.

	Signal	Count rate (s^{-1})	Measuring time (s)
Collision-induced fluorescence (L)	$L^{on}(\nu_0)$	9 460	180
	$L^{on}(\nu_0+\Delta\nu)$	8 940	180
	$L^{off}(\nu_0)$	8 930	50
	$L^{off}(\nu_0+\Delta\nu)$	8 840	50
Direct fluorescence (K)[a]	$K^{on}(\nu_0)$	4 440	50
	$K^{on}(\nu_0+\Delta\nu)$	590	50
	$K^{off}(\nu_0)$	11 200	30
	$K^{off}(\nu_0+\Delta\nu)$	520	30
Cross section $Q_{l\leftarrow k}^{|M_k|} = 0.70$ Å^2	$\frac{I_l}{I_k}$	0.127 ± 0.07	620

[a] Including neutral density filter (7×10^{-5} transmission).

which would be very hard to determine. Again, any unknown common factors are eliminated from Eq. (10). Even the potentially troublesome attenuation phenomenon factors out, to first order. We will now discuss, separately, the various quantities in Eq. (10) and the way in which the experiment has been calibrated with regard to each of them.

B. Secondary beam density n_2

The secondary-beam density n_2 is directly related to the source density $n_{2,0}$ through the shape of the radially expanding flow field of the supersonic expansion. For monoatomic gases, with the nozzle shape used in our setup, experiment and theory are in excellent agreement.[25] For a nozzle radius R_n, we have in spherical coordinates relative to the nozzle:

$$n_2(r,\theta) = n_{2,0}(aR_n/r)^2 \cos^3\theta \qquad (11)$$

with $a = 0.806$. (For a view of the coordinate system used in relation with the experiment, see Fig. 6.) The source density may be expressed in terms of the reservoir pressure $p_{2,0}$ and temperature $T_{2,0}$ by the ideal gas law.

In Fig. 7 we have plotted the ratio I_l/I_k of collision-induced and direct fluorescence signals, as a function of secondary-beam reservoir pressure $p_{2,0}^{\mathrm{He}}$. The linear dependence of $I_l/I_k \sim n_2 l_\tau Q_{l\leftarrow k}$ on $p_{2,0}^{\mathrm{He}}$ provides convincing evidence of the soundness of the principles embodied in our experiment. In addition, of course, the linear dependence of n_2 itself on $p_{2,0}$ is demonstrated in this way, indicating our control of secondary-beam properties. In practice, at large distance from the nozzle, the effect of residual pressure (due to limited pumping capacity) is bound to make itself felt.

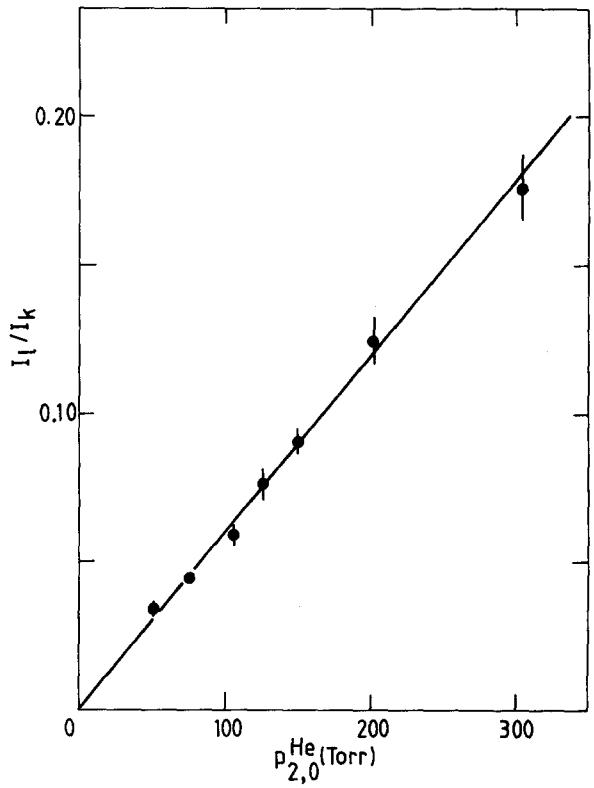

FIG. 7. Collision induced to direct fluorescence ratio I_l/I_k as a function of the secondary-beam reservoir pressure $p_{2,0}^{\mathrm{He}}$. In accordance with Eq. (9), I_l/I_k does not depend on the primary-beam transmission factor T_k, but is proportional to $n_2 \sim p_{2,0}$.

C. Transmission factor T_k

The attenuation of the primary beam, traveling in the x direction, by secondary-beam particles can be described by a transmission factor $T_k(x) = n_{\mathrm{Ne}^*}(x)/n_{\mathrm{Ne}^*}(-\infty)$, of the form [compare Eq. (3)]

$$T_k(\mathbf{r}) = \exp\left(-\int_{-\infty}^{x} \frac{g(\mathbf{r})}{v_1} n_2(\mathbf{r}) Q^{\mathrm{el}}\, dx'\right). \qquad (12)$$

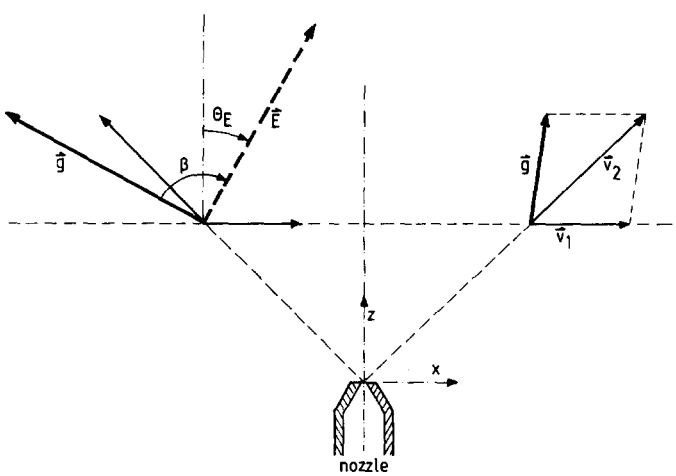

FIG. 6. Newton diagram of the collision process, with $\mathbf{v}_1$ and $\mathbf{v}_2$ the primary- and secondary-beam velocities. The laser beam is in the y direction. The laser electric field vector E makes an angle β with the relative velocity g.

Here Q^{el} is the effective total cross section for elastic scattering of Ne* atoms. Assuming monoenergetic particle beams and with the secondary-beam density given by Eq. (11), Eq. (12) can be solved analytically in the xz plane, determined by the primary-beam axis (x) and the center line (z) of the secondary-beam expansion (see Fig. 6).[36] Of course, at any given position we are bound to find

$$-\ln(T_k) \sim n_{2,0} \sim p_{2,0}.$$

This behavior of T_k as a function of the secondary-beam pressure $p_{2,0}$ is indeed demonstrated in Fig. 8. Figure 9 shows T_k as a function of the position x_l of the laser beam along the primary-beam axis. A curve fit on the basis of Eq. (12) to Ne**–He transmission data for a variety of pressures and positions (x,z) yields a value $Q^{\mathrm{el}}_{\mathrm{Ne}^*\text{-He}} \simeq 100$ Å^2. This is a reasonable value for hard-sphere scattering, as shown by comparison with $\pi R_m^2 \simeq 75$ Å^2, with R_m the position of the potential well.[37] The residual gas pressure within the parabolic mirror, found from these measurements as $p_{r,\mathrm{He}} \simeq 4\times10^{-4}$ Torr for $p_{2,0} = 120$ Torr, corresponds closely with the value $p_{r,\mathrm{He}} \simeq 7\times10^{-4}$, calculated on the basis of pumping speed considerations.

D. Optimum collision-induced fluorescence signal I_l

For a given position of the scattering volume, the collision-induced fluorescence signal I_l is determined by the product $T_k n_2$ of primary-beam transmission and secondary-beam density [see Eq. (10), or Eqs. (3) and (4)]. As an increase in n_2 automatically results in a decrease in T_k, there

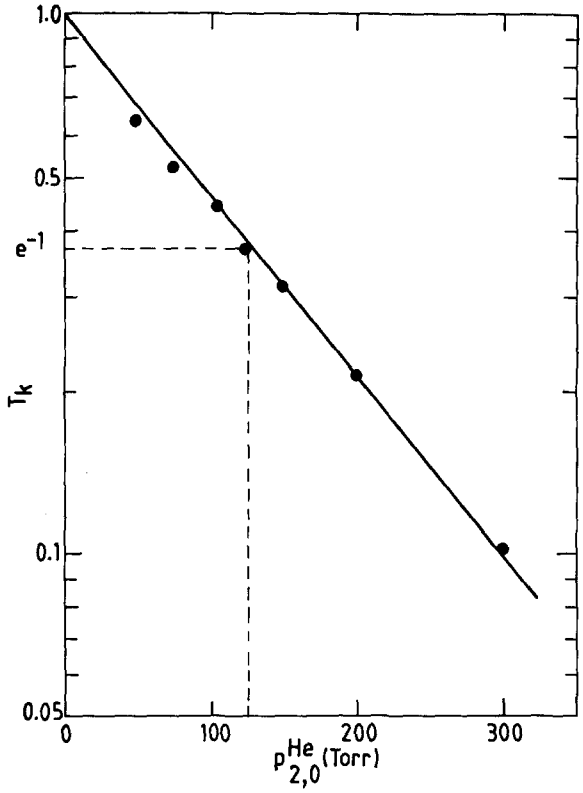

FIG. 8. The primary-beam transmission factor T_k as a function of the secondary-beam reservoir pressure $p^{He}_{2,0}$. The observed exponential attenuation conforms to Eq. (12). The $1/e$ point corresponds to the optimum of I_f in Fig. 10.

is bound to be an optimum reservoir density $n_{2,0}$, for which I_f attains a maximum value. This occurs, when

$$\frac{\partial I_f}{\partial n_{2,0}} = \frac{\partial (T_k n_2)}{\partial n_{2,0}} = 0. \tag{13}$$

Behavior of this kind can be observed in Fig. 10 of I_f vs the secondary-beam reservoir pressure $p^{He}_{2,0} \sim n_{2,0}$. If in Eq. (12) for T_k the factor g/v_1 is neglected, it can be readily verified that for $x = 0$ the optimum reservoir density is given by

$$n^{opt}_{2,0} = \frac{3z_n}{2(aR_n)^2 Q^{el}}. \tag{14}$$

At room temperature this coresponds with $p^{opt}_{2,0} = 110$ Torr for $Q^{el} = 100$ Å^2 and $R_n = 25$ μm. Figure 10 which shows the optimum to lie at $p^{opt}_{2,0} \simeq 120$ Torr bears this out. For the above value of $n^{opt}_{2,0}$, we have $T^{opt}_k \simeq 1/e$. This is confirmed by Fig. 8 of $T_k(p^{He}_{2,0})$!

E. Center-of-mass energy E

The center-of-mass energy is given by $E = \frac{1}{2}\mu g^2$, with μ the reduced mass and g the relative velocity of the colliding particles. Into g enter both the primary-beam velocity $\mathbf{v}_1$ and the secondary-beam velocity $\mathbf{v}_2$.

As to v_2, the velocity distribution in our supersonic expansion is given by Ref. 25. It is approximately Gaussian, peaked at the final value of the flow velocity:

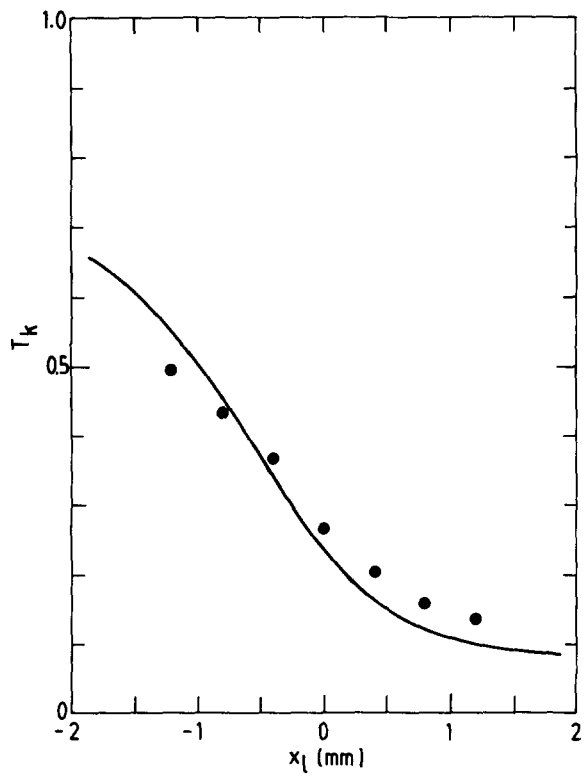

FIG. 9. The primary-beam transmission factor T_k as a function of the laser-beam position x_l along the primary-beam axis. The agreement with the calculated transmission is less than usual for this measurement. This has a negligible effect on calculated cross sections, however.

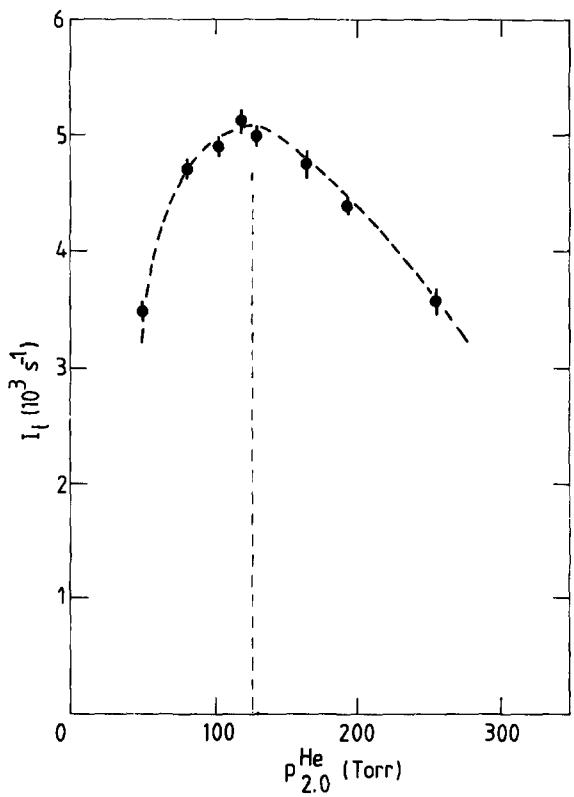

FIG. 10. The collision-induced fluorescence signal I_f as a function of secondary-beam reservoir pressure $p^{He}_{2,0}$. Due to the opposite effect of $p^{He}_{2,0}$ on the secondary-beam density n_2 and the primary-beam transmission factor T_k, an optimum pressure is found. This roughly satisfies Eq. (14) and corresponds to $T_k \simeq 1/e$ in Fig. 8.

$$v_2 = u_\infty (1 - \tfrac{1}{2} S^{-2}),$$
$$u_\infty = \left(\frac{\gamma}{\gamma - 1}\right)^{1/2} \left(\frac{2kT_{2,0}}{m_2}\right)^{1/2}, \quad (15)$$

where γ represents the specific heat ratio $\gamma = c_p/c_V$ (5/3 for monoatomic gases). At a typical pressure $p_{2,0}^{He} = 120$ Torr and temperature $T_{2,0} = 300$ K, the speed ratio for He is $S_2^{He} = 4.4$, resulting in $v_2^{He} = 0.97\, u_\infty = 1715$ m s^{-1}. For Ne, at $p_{2,0}^{Ne} = 160$ Torr, we find $S_2^{Ne} = 6.5$, so that $v_2^{Ne} = 0.99\, u_\infty = 775$ m s^{-1}.

Equation (15) will not serve for the primary-beam velocity v_1, for lack of an appropriate temperature $T_{1,0}$ in the discharge-excited source. Therefore, time-of-flight (TOF) measurements were performed to determine the primary-beam velocity distribution. For a pure 100% Ne discharge, the result is given in Fig. 11(a). A 15% Ne–85% He seeded beam yields the TOF spectrum of Fig. 11(b). In both cases the TOF spectrum was fitted with a Gaussian velocity distribution. The peak velocity v_1 and speed ratio S_1 are found to be $v_1 = 1010$ m s^{-1} and $S_1 = 4.7$ for the pure beam, while $v_1 = 1495$ m s^{-1} and $S_1 = 5.7$ for the seeded beam.

We note that the position dependence of the direction of $\mathbf{v}_2$ causes both magnitude and direction of the relative velocity to be position dependent, as well. This is illustrated in Fig. 6 by the xz diagram of velocity vectors in the laboratory system.

F. Optical detection efficiency η

The optical detection system and its components have been described above. The detection efficiency η_l (defined as pulses counted per photons produced) may be written as

$$\eta_l = \sum_j \frac{A_{lj}}{A_l} \eta_j^0(\lambda_j) \eta_j(\mathbf{r}, \theta_E). \quad (16)$$

Here A_{lj}/A_l is the branching ratio for a particular fluorescence line j. In addition to the quantum efficiency of the photomultiplier, the total transmission along the optical axis of all elements is featured in η_j^0. Position-dependent deviations from the optical axis (associated, for example, with nonnormal incidence on the interference filters), as well as the effect of nonisotropic light production by polarized atoms, are incorporated in η_j. With an interference filter in the optical system, the sum in Eq. (16) is usually reduced to a single term $j = l$, the only one for which $\eta_j^0 \neq 0$.

We have calibrated each optical component separately. Subsequently, the geometric function η_j is calculated numerically. Typical transmission curves for a three-cavity interference filter [692.9 nm, corresponding to the $\{\alpha\}_6 \rightarrow (^1P_1)$ transition], a red glass cutoff filter (645 nm, and a neutral density filter, are given in Fig. 12. They have been measured using a standard light source, a Jarrell–Ash

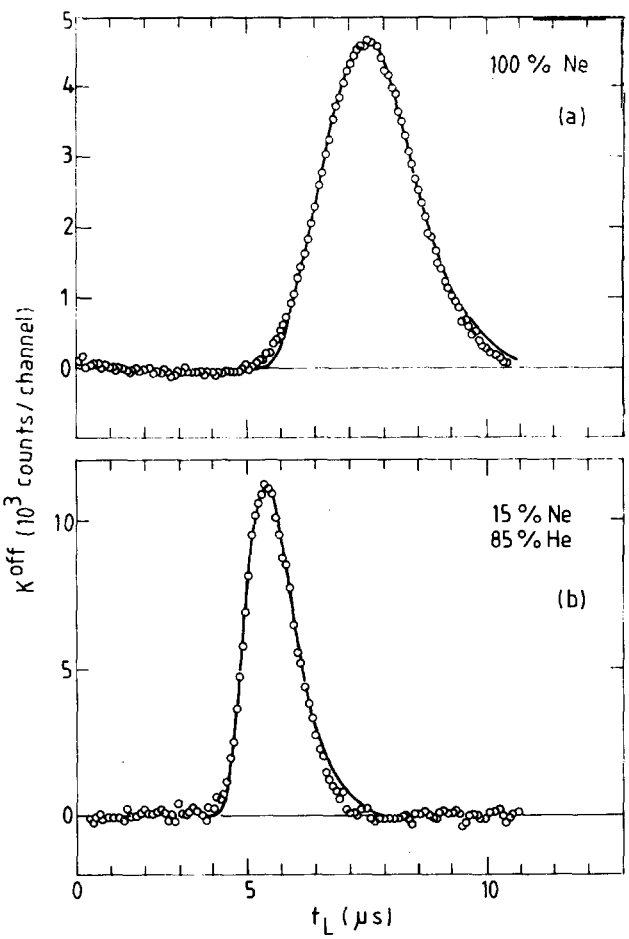

FIG. 11. Time-of-flight distributions of a 100% Ne (a) and a 15% Ne–85% He (b) beam from the thermal metastable beam source. The flight path is $L \simeq 86$ mm. Both spectra were obtained with the laser chopper operating in single-burst mode, with channel-time $t_k = 1$ μs. Peak velocities are $v_1^{pure} = 1010$ ms^{-1} and $v_1^{seeded} = 1495$ ms^{-1}.

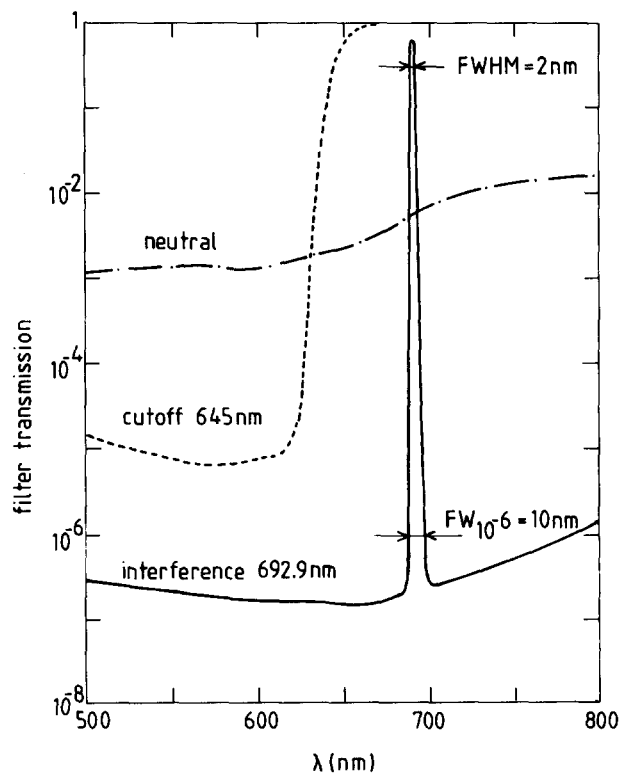

FIG. 12. Transmission as a function of wavelength for a 692.9 nm interference filter, a 645 nm red glass cutoff filter, and a neutral density filter. These filters are typical of the filters used in the experiment.

1.0 m double (Czerny–Turner) monochromator and a Keithley Instruments 610 CR electrometer. The curve for the interference filter was obtained under conditions of normal incidence. For nonnormal angles of incidence, the transmission profile is shifted to lower wavelengths. This means, that the nominal wavelength will be transmitted to a lesser degree. The latter effect is exemplified by Fig. 13 of the transmission of the 692. 9 nm signal line (from a neon spectral lamp) through the interference filter of Fig. 12, as a function of the off-normal angle of incidence α. Taking the other optical components (parabolic mirror, light-guide, lens) into account as well, we find the calculated position dependence $\eta(r,z)$ of the detection efficiency for this interference filter to be as in Fig. 14. In the calculation, isotropic emission of light was assumed.

The anisotropy of the detection efficiency becomes apparent, when measuring I_k for varying angles θ_E of the laser polarization. The influence of the nonisotropic emission of dipole radiation by the polarized initial state $\{\alpha\}_k$ (see Sec. IV H) causes I_k to vary. For a Ne*($^3P_0$) metastable state, this is shown in Fig. 15. Again, the effect is largely reproduced by the appropriate calculation.

G. Alignment of three crossing beams

The experiment requires that the primary-beam axis and the center line of the secondary-beam expansion cross at right angles, at or near the focal point of the parabolic mirror. The laser beam must cross the primary beam, once more at right angles, in a spot well determined with respect to the secondary-beam nozzle. It is relatively straightforward to first align the two primary-beam defining diaphragms with the focal point of the mirror, and then the skimmer of the primary-beam source with the diaphragms; also, to make the secondary-beam nozzle axis coincide with that of the mirror. All these components may then be fixed in place semipermanently. Laser-beam alignment, however, is another matter.

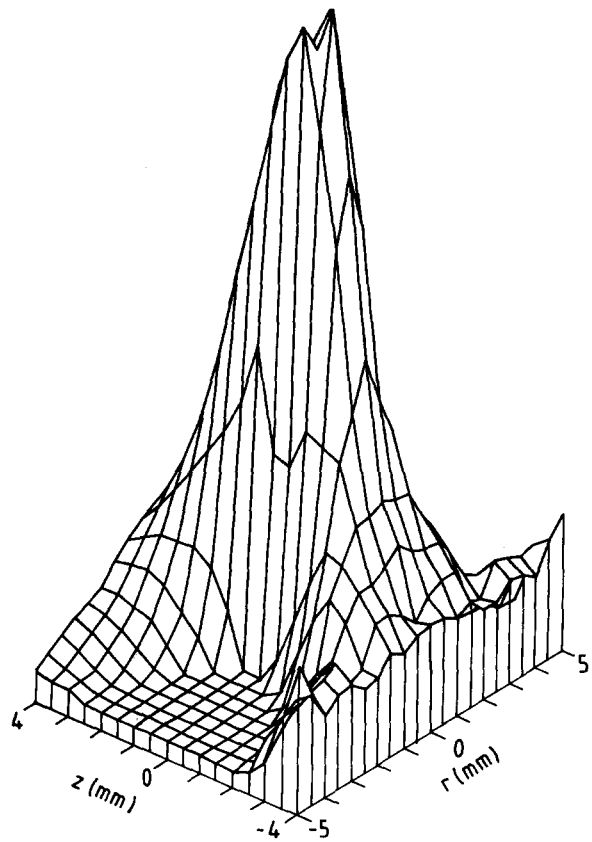

FIG. 14. Calculated detection efficiency $\eta(r,z)$ of the optical system with the interference filter of Figs. 12 and 13. Isotropic emission of fluorescence radiation has been assumed. The axial symmetry about the vertical z axis then makes η a function of $r = (x^2 + y^2)^{1/2}$ and z only, where the origin is in the focus of the parabolic mirror.

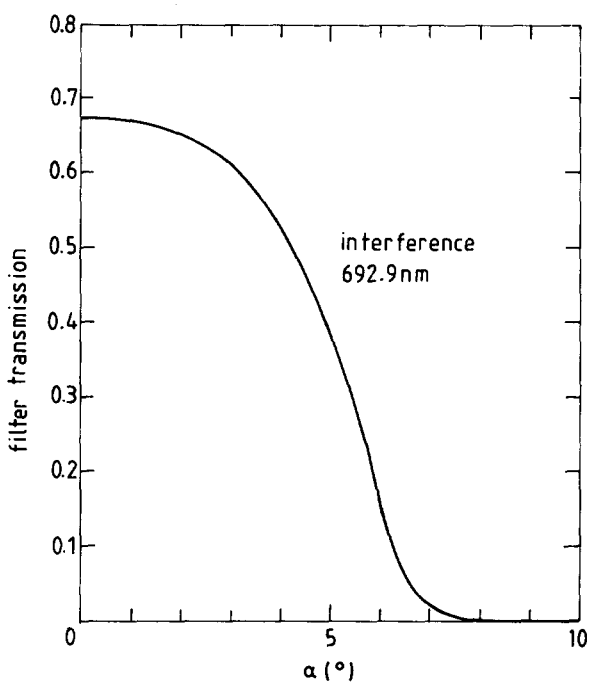

FIG. 13. Transmission of the 692.9 nm signal line through the 692.9 nm interference filter of Fig. 12, as a function of the off-normal angle of incidence α. In effect, the transmission peak shifts to lower wavelengths with increasing α.

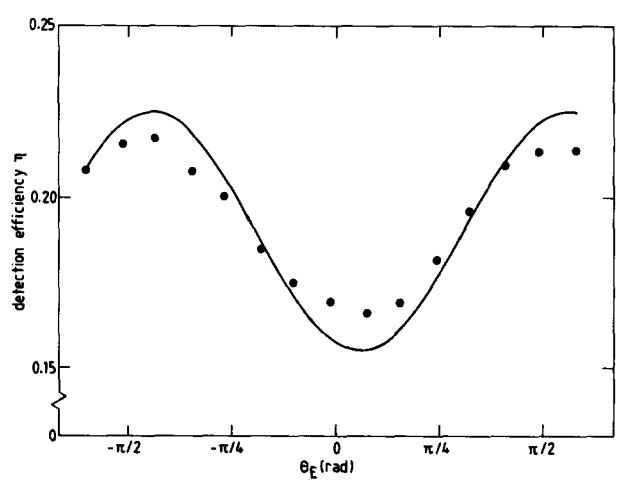

FIG. 15. The direct fluorescence signal K^{off} for the ($\{\alpha\}_5;J_5 = 1$) state excited from the metastable ($^3P_0$) state, as a function of the laser polarization angle θ_E with the z axis (the symmetry axis of the optical system). Taking account of the anisotropy of the fluorescence radiation, the less than 4π solid-angle detection efficiency, and the off-axis laser-beam position, the calculated drawn curve reproduces the signal well.

As a characteristic of our use of a free-jet secondary-beam expansion, the laser beam ultimately determines the position of the collision volume. As the relative velocity g and the secondary-beam density n_2 in particular are strongly position dependent, laser-beam alignment takes on a critical importance. This is evidenced by Fig. 16 of an I_l signal as a function of the laser-beam position x_l along the primary-beam axis, and likewise by Fig. 17 of the ratio I_l/I_k.

In the interest of accuracy and reproducibility, the laser line has been fixed with two quadrant detectors, as described earlier. Theoretical accuracy of the horizontal laser-beam alignment is $\Delta x = 0.005$ mm and $\Delta\varphi = 0.1$ mrad, as determined by the step size (0.01 mm and 0.2 mrad, respectively) of the stepper-motor-gearing combination selected for the laser-beam translator/rotator module. By the automated alignment procedure of Sec. III the stepper-motor setting for the angle φ is reproduced perfectly every time, that for the position x within two steps ($\Delta x = 0.02$ mm). Figures for the vertical z position are similar to those for the x position.

In the matter of the initial laser-beam alignment, i.e., the positioning of the quadrant detectors, the top of the nozzle provides both a vertical and (to a lesser degree) a horizontal visual reference. Perpendicularity of laser and primary beam can be easily achieved by measuring the direct fluorescence

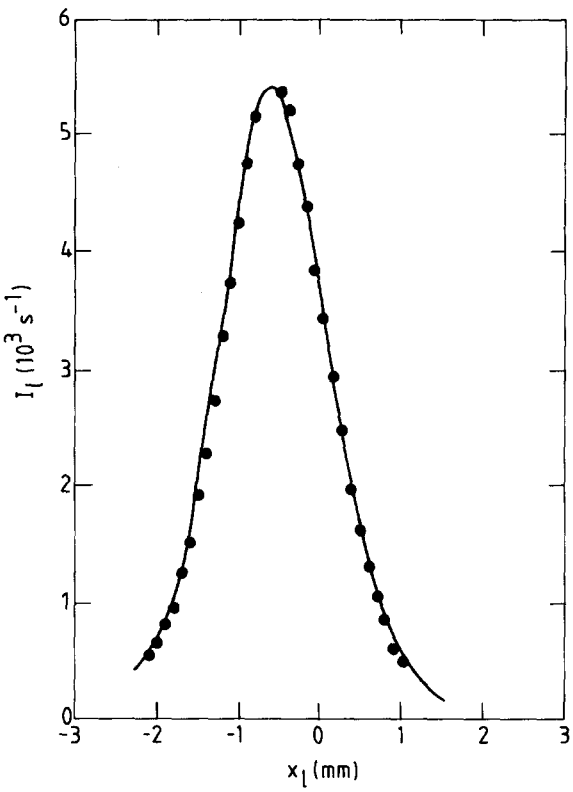

FIG. 16. The collision-induced fluorescence signal I_l resulting from the Ne**–He$\{\alpha\}_5 \rightarrow \{\alpha\}_4$ transition, as a function of the laser-beam position x_l along the primary-beam axis. The drawn curve was calculated according to Eq. (10) and normalized to the maximum of the experimental data. The lack of a significant polarization effect in the $\{\alpha\}_5 \rightarrow \{\alpha\}_4$ cross section (see Fig. 27) obviates the need for a correction for the changing angle β between the laser electric field E and the relative velocity g. What small polarization effect there is tends to compensate the effect of the energy change associated with a change in x_l (compare Fig. 17).

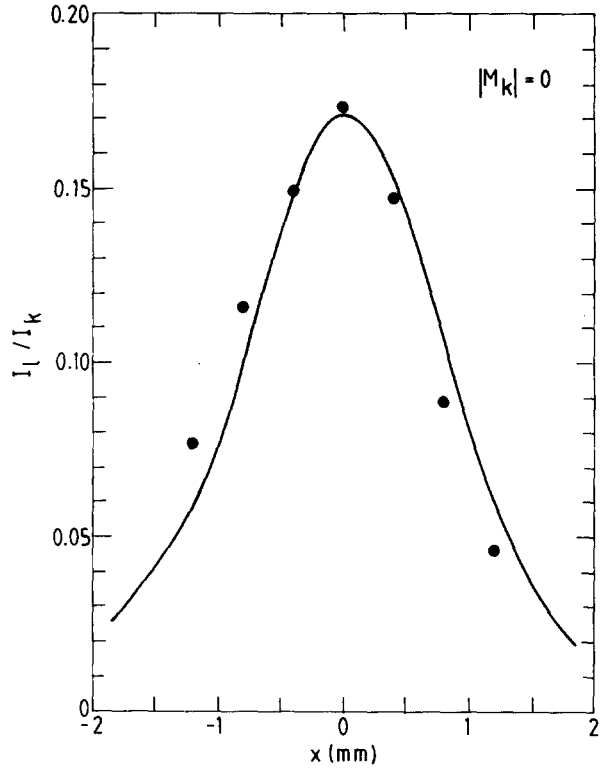

FIG. 17. Collision-induced to direct fluorescence ratio I_l/I_k for the Ne**–He$\{\alpha\}_5 \rightarrow \{\alpha\}_7$ transition for $|M_5| = 0$, as a function of the laser-beam position x_l along the primary-beam axis. The drawn curve was calculated according to Eq. (10) and normalized to the maximum of the experimental data. The result reflects the energy dependence of $Q^{|0|}_{7\leftarrow 5}$ that is shown in Fig. 32. The higher energy upstream of the secondary-beam nozzle corresponds to a larger cross section and thus to a larger fluorescence signal. Downstream of the nozzle the reverse is true.

signal I_k over a wide range of angles φ, with a figure like Fig. 18 as the result. The correct setting corresponds to the maximum signal (minimum Doppler shift). In a similar way the vertical laser-beam position may be checked for maximum overlap with the primary beam.

In a somewhat more elaborate procedure, the experiment itself provides an additional check on the horizontal position. We can perform a so called polarization measurement of the cross section $Q^{\beta}_{l\leftarrow k}$ for an $|\alpha_k J_k = 1>$ initial state, excited from the ($^3P_0$) metastable state. Here β is the angle between the electric field vector E of the linearly polarized laser and the asymptotic relative velocity. Theory[21] predicts that the observed cross section will behave according to

$$Q^{\beta}_{l\leftarrow k} = C^1_0 + C^1_1 \cos 2\beta. \tag{17}$$

In principle, any transition of the above description will do. In practice, the Ne**–He $\{\alpha\}_5 \rightarrow \{\alpha\}_7$ transition is a most convenient candidate, due to its large polarization effect combined with a considerable cross-section magnitude.

The cross section $Q^{\beta}_{l\leftarrow k}$ is measured by variation of the angle θ_E between the primary-beam velocity $\mathbf{v}_1$ and E. As may be seen in Fig. 6 of the diagram of velocity vectors in the laboratory system, the relation between θ_E and β depends on the position x_s of the scattering center. In accordance with Eq. (17), extrema will occur at angle $\theta_E = \theta_0$ and $\theta_E = \theta_0 + \pi/2$. This we observe in Fig. 19. These extrema cor-

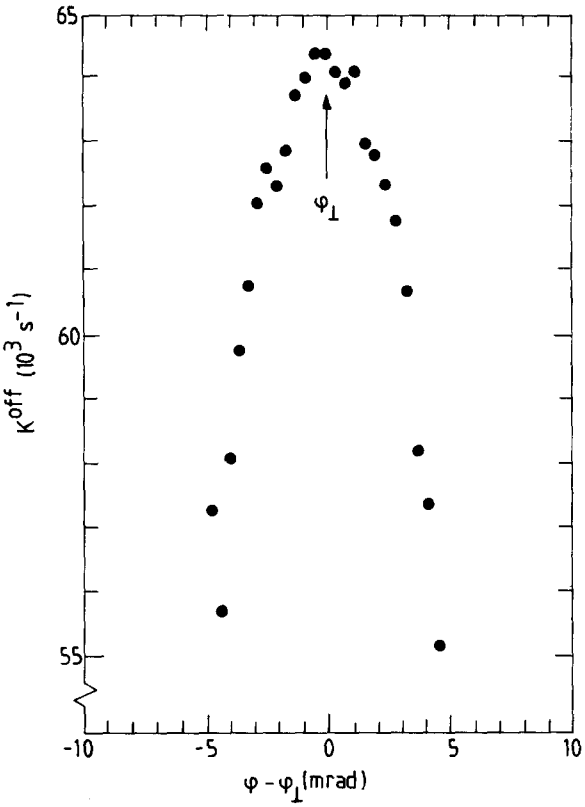

FIG. 18. The direct fluorescence signal K^{off} as a function of the angle φ between laser and primary beam. With the laser tuned to the frequency of a Doppler-free atomic transition, the signal's maximum corresponds to perpendicular alignment. For increasing misalignment the Doppler shift grows and the fluorescence signal decreases.

respond to $\beta = 0$ and $\beta = \pi/2$. We only need to identify the extremum belonging to $\beta = 0$, for which $\theta_E = \theta_g$, i.e., $\mathbf{g} \| \mathbf{E}$. This problem can be solved unequivocally by measuring $Q_{l \leftarrow k}$ for some different positions x_s and, if necessary, primary-beam velocities v_1.

Referring to Fig. 6, the absolute value of the relative velocity vector $\mathbf{g}$ can be readily calculated from the orientation θ_g, using the well-known values of v_1 and v_2 as input. So can the orientation of $\mathbf{v}_2$. The latter, in combination with the nozzle-to-primary-beam distance z_n, gives us the effective position x_s of the collision volume on the primary-beam axis. The laser-beam position x_l then follows from the offset $\Delta x_{ls} = x_l - x_s$, specific to the optical pumping process. Over a number of such tests, the x scale is permanently coupled to the scale of the laser-beam translator or, in our case, to the quadrant detectors.

H. Optical pumping

Because the distribution of the initial $\{\alpha\}_k$ atoms ultimately determines the position and extent of the collision region, its calculation is of prime importance. We have numerically solved a set of rate equations for the upper Ne**$\{\alpha\}_k$ and lower Ne*($^3P_{0,2}$) level densities, taking into account absorption, stimulated emission, and spontaneous emission [the latter to all Ne*$\{(2p)^5(3s)\}$ levels]. The different upper and lower magnetic sublevels m_J, with respect to the laser polarization E, are treated separately. Also, it is possible to postulate a magnetic field.

Among the simplifications of our model are: (1) the divergence of the Ne* and laser beams is neglected; (2) they are taken to be perpendicular; (3) the laser is tuned exactly to the optical transition. Thus, with the Ne* atoms moving in the x direction, we have essentially a one-dimensional problem. For every value of z, we find a number of $J_k + 1$ density profiles $n_k^{|m_k|_E}(x)$. We usually assume a perfectly Gaussian two-dimensional laser field, very slightly collimated. Figure 20 of a laser-intensity profile, with a Gaussian fit, bears out this assumption. Disregarding in the present context both magnetic sublevels and magnetic fields (which are discussed below), we find for instance a profile $n_k(x)$ such as shown in Sec. V A. With the laser beam used in the experiment (power $P \simeq 0.1$ mW, waist radius $[1/e^2]W_x = W_z \simeq 0.5$mm) and at thermal velocities, the short-lived Ne**$\{\alpha\}_k$ atoms are confined to a considerably smaller space than the laser-beam profile itself. Also, note the upstream shift of the n_k profile. [All this, of course, does not hold for the two-level Ne*($^3P_2$)–Ne**$\{a\}_9$ system.] A comparison between scattering volume positions, determined from polarization measurements (Sec. IV G) on the one hand, and calculated from laser-beam positions on the other,

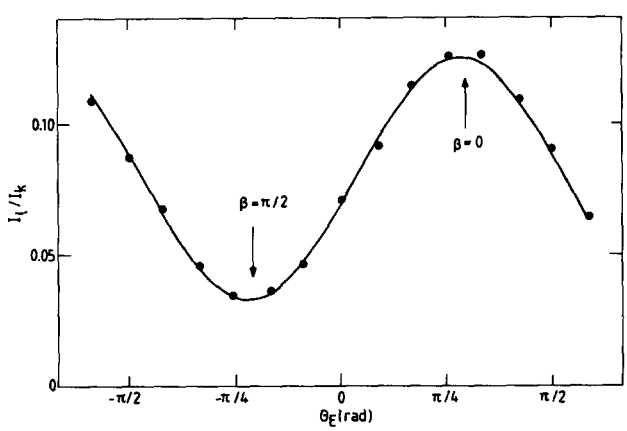

FIG. 19. The ratio I_l/I_k of collision-induced and direct fluorescence signals for the Ne**–He$\{\alpha\}_5 \rightarrow \{\alpha\}_7$ transition, as a function of the laser-polarization angle θ_E. The drawn curve results from a least-squares fit of the data to Eq. (17). This offers a way of determining the position of the scattering center along the primary-beam axis.

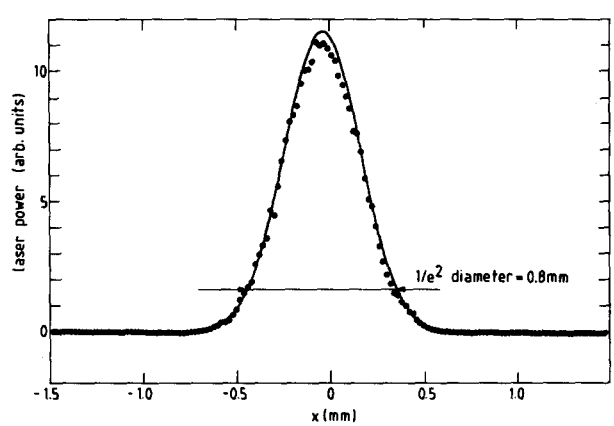

FIG. 20. Horizontal intensity profile of the laser beam in the scattering center. The drawn curve represents a Gaussian profile of 0.8 mm waist diameter ($1/e^2$).

confirms that these calculations basically represent reality well.

A magnetic field exerts a certain influence on the effective scattering center position. Much more important, though, is its effect on the observed cross sections $Q^{\beta}_{l\leftarrow k}$. We recall that the ultimate purpose of the experiment is to determine single-M_k-state polarized cross sections $Q^{|M_k|}_{l\leftarrow k}$, where M_k is the magnetic quantum number of the initial electronic angular momentum **J** along the asymptotic relative velocity **g**. Now, the observed cross section Q^{β}, with β the angle between **E** and **g**, has the general form

$$Q^{\beta}_{l\leftarrow k} = \sum_{n=0}^{J_k} C^{J_k}_{n} \cos 2n\beta. \tag{18}$$

In detail,[20]

$$Q^{\beta}_{l\leftarrow k} = \sum_{m_k=-J_k}^{J_k} g_{m_k} \sum_{M_k=-J_k}^{J_k} \{d^{J_k}_{m_k M_k}(\beta)\}^2 Q^{|M_k|}_{l\leftarrow k}, \tag{19}$$

where the rotation matrices or reduced Wigner-D-functions d[38] transform the initial distribution g_{m_k} over magnetic substates $|\alpha_k J_k m_k\rangle_{\mathbf{E}}$ to a distribution over substates $|\alpha_k J_k M_k\rangle_{\mathbf{g}}$. The calculation of the distribution g_{m_k} provides the final calibration of the experiment.

The general principles involved have been mentioned already in our discussion of the initial-state density profile $n^{m_k}_k(\mathbf{r})$. In the present experiment, the distribution parameter g_{m_k} may be linked to the time integral of $n^{m_k}_k$ over the collision region. Here, the presence or absence of a magnetic field makes a crucial difference.[27] With a linearly polarized laser, only $\Delta m = 0$ transitions are allowed. The case of an $|\alpha_k J_k = 1\rangle$ initial state being excited from the $|^3P_0, J_i = 0\rangle$ metastable state is straightforward. Only the $m_k = 0$ substate is populated. Due to the upper state's short lifetime, no appreciable precession of $\mathbf{J}_k$ about a magnetic field **B** of earth-field's strength can take place. As a result, we find

$$g^{J_k=1}_{m_k=0} = 1,$$
$$g^{J_k=1}_{|m_k|=1} = 0. \tag{20}$$

For Eq. (19) this implies, simply, that

$$Q^{\beta}_{l\leftarrow k} = \tfrac{1}{2}(Q^{|0|}_{l\leftarrow k} + Q^{|1|}_{l\leftarrow k}) + \tfrac{1}{2}(Q^{|0|}_{l\leftarrow k} - Q^{|1|}_{l\leftarrow k})\cos 2\beta. \tag{21}$$

For $|\alpha_k J_k = 2\rangle$ and $|^3P_2, J_i = 2\rangle$, the $\Delta J = 0$, $\Delta m = 0$ transition is forbidden. However, while the upper short-lived state is quite impervious to the presence of a magnetic field **B**, the metastable lower state is not. Mixing of the metastable $m_i = 0$ substates takes place, and the distribution $g^{J_k=2}_{m_k}$ over short-lived m_k substates depends on the field's magnitude and its direction with respect to the laser polarization **E**:

$$g^{J_k=2}_{m_k=0} = 0,$$
$$g^{J_k=2}_{|m_k|} = g^{J_k=2}_{|m_k|}(\mathbf{B}). \tag{22}$$

This is demonstrated by Fig. 21 of the evolution in time of $n^{|m_k|}_k$ for the $\{\alpha\}_4$ state, with and without a magnetic field. To judge the extent to which a magnetic field complicates the analysis of Q^{β}, it must be kept in mind that during the experiment the angle between **B** and **E** changes continuously. The distribution $g^{J_k=2}_{m_k}$ will vary accordingly. This produces the asymmetry in, for example, the $Q^{\beta}_{7\leftarrow 8}$ cross section of Fig. 22, contrary to Eq. (18)! Evidently, while for some states $|\alpha_k J_k = 2\rangle$ it matters less than for others, the absence of a magnetic field offers much the best starting point for the analysis of observed cross sections.

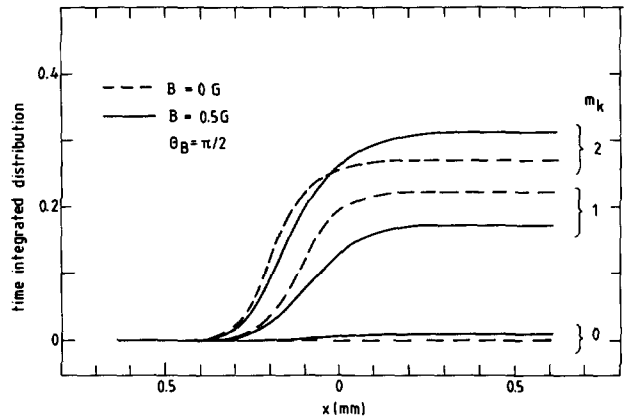

FIG. 21. The time-integrated upper-state density $n^{|m_k|}_8(t)$, resulting from the $(^3P_2) \rightarrow \{\alpha\}_8$ excitation process, calculated with and without a magnetic field **B**. Here θ_B is the angle between **B** and the laser electric field **E**. The influence of B, when not compensated for, carries over directly into observed cross sections!

In our experiment the conditions are very favorable for the successful compensation of whatever magnetic field is present. First, the size of the scattering volume is so small ($\simeq 1$ mm^3), that only limited demands are made of the compensating field's homogeneity. More importantly, the optical pumping process itself offers and inbuilt verification method for the success of the compensating efforts.

For this, an $|\alpha_k J_k = 1\rangle$ state is excited from the metastable $|^3P_2, J_i = 2\rangle$ state. With the laser linearly polarized, as ever, only the lower level's $m_i = -1, 0, 1$ magnetic substates are pumped. In the absence of a magnetic field, the $m_i = -2, 2$ substates will be unaffected. Under those circumstances and sufficiently close to saturation, an isotropic dis-

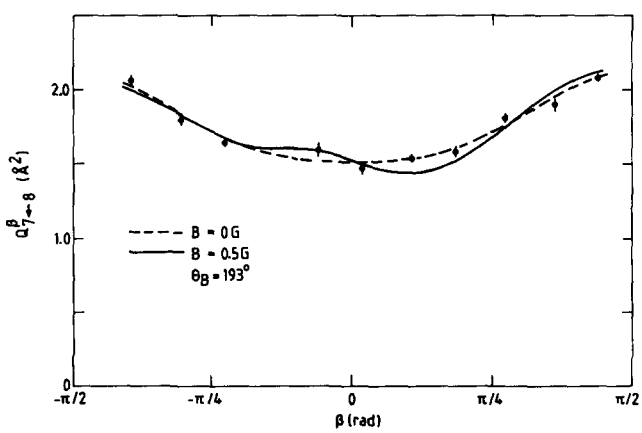

FIG. 22. For varying orientation θ_E of the laser electric field vector **E**, the angle θ_B of the magnetic field **B** with **E** varies also. This causes the distribution over magnetic substates $|\alpha_k J_k m_k\rangle_E$ to change continuously. In the observed Ne**–He cross section $Q^{\beta}_{10\leftarrow 8}$ as a function of the angle β between **E** and the relative velocity **g**, a marked deviation from Eq. (18) is the result.

tribution over the upper level's magnetic substates will be the result:

$$g^{J_k=1}_{m_k=0} \simeq 1/3,$$
$$g^{J_k=1}_{|m_k|=1} \simeq 1/3. \tag{23}$$

An unpolarized initial short-lived state must of course lead to an unpolarized cross section:

$$Q^{\beta}_{l\leftarrow k} = 1/3(Q^{|0|}_{l\leftarrow k} + 2Q^{|1|}_{l\leftarrow k}). \tag{24}$$

Now, any mixing of the $m_i = -2, 2$ substates due to a magnetic field is bound to give rise to a larger observed direct fluorescence signal I_k. Of course, if the magnetic field happens to be along the laser electric field **E**, no mixing will take place.

As mentioned in Sec. III, we have installed three sets of rectangular Helmholtz-like coils around the major x, y, and z axes of the experiment. They have been placed outside the vacuum chamber. Spatial limitations have forced us to deviate from the coils' ideal dimensions. Given the small scattering volume, this is of little significance.

Magnetic field compensation is best performed at a laser power sufficiently close to saturation that nearly all the relevant metastable atoms are pumped. Care must be taken that the laser polarization is not along the field's component being compensated at the time. Successive and iterative minimization of the direct fluorescence signal I_k then yields the correct compensating field. The ultimate test for this procedure is provided by the comparison, shown in Fig. 23, of the signal I_k for the $\{\alpha\}_5$ state [excited from the $(^3P_2)$ state], measured with and without activated coils, as a function of the laser polarization angle θ_E. Whereas the fluorescence yield is seen to vary strongly (about 20%) under the local field conditions, it is much more constant (to within 4%) when the compensating field is turned on, in accordance with Eq. (24). Moreover, the minimum signals are the same in both cases! At the time of this measurement the local field's strength was about $B \simeq 0.5$ G.

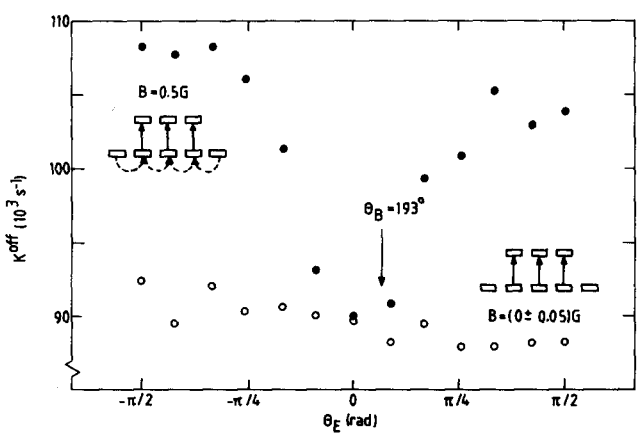

FIG. 23. The direct fluorescence signal K^{off} for the $(\{\alpha\}_5, J_5 = 1)$ state excited from the metastable $(^3P_2)$ state, as a function of the laser-polarization angle θ_E. A magnetic field in the scattering center causes the signal to vary, due to the admixture of the $|^3P_2, J = 2, m_J = \pm 2\rangle_E$ sublevels. The nearly constant signal testifies to the absence of a magnetic field. Note the enlargement of the vertical scale.

V. INELASTIC TOTAL CROSS SECTIONS

A. Deconvolution for finite scattering volume

We can express Eq. (10) for the ratio I_l/I_k of collision-induced and direct fluorescence signals in terms of the ideal first-order expression of Eq. (9), through a convolution factor ξ_V:

$$\frac{I_l}{I_k} = \xi_V \left(\frac{I_l}{I_k}\right)_{\text{ideal}}. \tag{25}$$

Here $(I_l/I_k)_{\text{ideal}}$ is to be calculated in the scattering center $\mathbf{r}_{sc}$, for which we take the center-of-gravity of the $\{\alpha\}_l$ transition. The various elements making up I_l/I_k have been treated more or less extensively in Sec. IV, with the exception of the cross section $Q_{l\leftarrow k}(g)$ itself. In general, we have

$$Q_{l\leftarrow k}(g) = f(g) Q_{l\leftarrow k}(g_{sc}),$$
$$f(g) = 1 + (g - g_{sc}) \left(\frac{dQ_{l\leftarrow k}}{dg}\right)_{sc} + \cdots. \tag{26}$$

The model function $f(g)$ is of less than critical importance, though, because of the small size of the collision region. Well suited for Ne**–He transitions at thermal energies appears to be the function

$$f(g) = \frac{g}{g_{sc}}. \tag{27}$$

With $f(g)$ figuring in ξ_V, we find from Eq. (25):

$$Q_{l\leftarrow k}(g_{sc}) = \left(\frac{I_l}{I_k}\right)_{\text{expt}} \Big/ \left\{\xi_V \left(\frac{\eta_l}{\eta_k} n_2 \frac{g}{v_1} l_\tau\right)_{sc}\right\}. \tag{28}$$

The I_l and I_k integrals of Eq. (10) are now approximated by means of a two-dimensional integration over the plane, which contains the primary-beam axis and is normal to the laser beam, i.e., the xz plane of Fig. 6. The primary and laser beams are presupposed to be cylindrical and exhibit maximum overlap. The effects of the primary beam extending in the laser beam's y direction are taken into account only through the primary-beam width itself, i.e., through a z-dependent weight factor. Since the secondary-beam density n_2 typically varies by less than 15% over the whole primary-beam width, the resulting overestimation of I_l is limited. Ultimately, of course, the integration area is determined by the position x_l of the laser beam.

The detection-efficiency profiles $\eta_l(x,z_f)$ (relative to the focal point $z_f = 0$ of the parabolic mirror) need to be calculated only once, for each of the available interference filters (disregarding, of course, possible variations in the anisotropy of the fluorescence radiation). For a grid of (x,z_f) values, the $\eta_l(x,z_f)$ have been permanently stored for use in the calculations. Likewise, the calculation of the density profile $n_k(x,z)$ of the initial short-lived $\{\alpha\}_k$ atoms is independent of the laser beam position x_l. Its results can be used for any combination of x_l, nozzle distance z_n and final state $\{\alpha\}_l$.

Figure 24 gives an example of the behavior of the various quantities in Eq. (10) as a function of x in the xz plane, for a given value of z. In Fig. 25, we show the shape of a calculated $\{\alpha\}_l$ distribution. It is confined to a relatively small region. The center-of-gravity (x_{sc},z_{sc}) generally does not lie on the laser-beam axis (x_l,z_n).

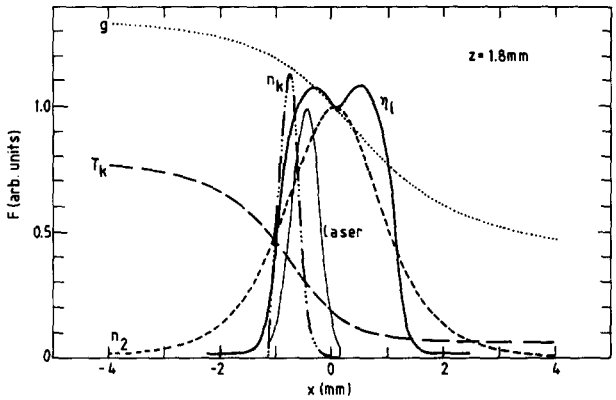

FIG. 24. The variation with the horizontal coordinate x of Fig. 6, for a fixed value $z = 1.8$ mm, of the two-dimensional model functions for the secondary-beam density n_2 [Eq. (11)], the primary-beam transmission T_k [Eq. (12)], the $\{\alpha\}_k$ density n_k (Sec. IV H, disregarding magnetic sublevels), the relative velocity g (Sec. IV E), and the optical detection efficiency η (Sec. IV F, for isotropic light).

The ultimate result of the I_l/I_k calculation [Eq. (10)] on the one hand, and the I_l/I_k measurement [Eq. (8)] on the other, is taken to be an absolute total cross section $Q_{l\leftarrow k}(E)$, with the energy $E = \frac{1}{2}\mu g^2(x_{sc},z_{sc})$ pertaining to the point (x_{sc},z_{sc}), all in accordance with Eq. (26). A typical value of the convolution factor ξ_V of Eqs. (25) and (28) would be $\xi_V \simeq 0.8$.

B. Measurement of inelastic cross sections

The nucleus of any of the experiments of the preceding section is the I_l/I_k measurement with its eight component measurements, as discussed in Sec. III. The inherent calibration method, implied by the measurement of ratios I_l/I_k only, goes a long way towards eliminating any long-term drift effects, to which the thermal metastable source in particular is prone. In addition, as a measure against linear drift during the I_l/I_k measurement itself, it pays to adopt a symmetrical order of basic measurements. In the notation of Sec. III, an example would be: K^{off}–K^{on}–L^{on}–L^{off}–L^{on}–K^{on}–K^{off} (with each of these consisting of a measurement with tuned and detuned laser). In this respect, it saves time to minimize the number of filter changes and secondary-beam on/off transitions.

The efficacy of these measures is demonstrated by Fig. 26 of a complete Ne**–He polarization measurement for the $\{\alpha\}_9 \rightarrow \{\alpha\}_7$ transition. By way of a standard extra precaution, the range of laser polarization angles has been covered in two series: 105°, −75°,..., 105° and −90°, −60°,..., 90°. The measurement is atypical in that the observed drift is unusually large. Still, the net I_l/I_k signal is nearly unaffected by this. In addition, the constant value of the transmission factor K^{on}/K^{off} is a guarantee of a constant secondary-beam density.

In practice, it is the measuring program executed by the experiment computer that supervises a complete run of the experiment. Beforehand, it prompts for and stores a table of the experimental parameters: order, number, and length of the basic measurements; the filters required; the nature of the main experimental variable; its range, etc. These, and others, are all saved in a data file on disk. Then the experiment runs its course, with the computer initiating changes in the laser frequency, actuating stepper motors, and so on. Before going to a new setting of, e.g., the polarization angle, the data from the previous I_l/I_k measurement are saved in the datafile. An overview of the data is printed out, together with the results of a preliminary analysis. A complete run is usually scheduled to take about 3 h. This is roughly the

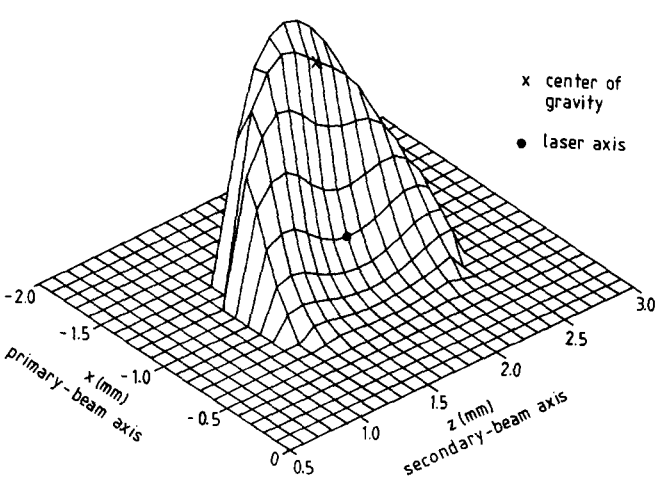

FIG. 25. Two-dimensional shape of the calculated collision-induced $\{\alpha\}_7$ distribution $n_7(x,z)$ for the Ne**–He$\{\alpha\}_5 \rightarrow \{\alpha\}_7$ transition, obtained from Eq. (10) with a supposed 1.3 mm diameter laser beam of 0.1 mW power. The distribution's center-of-gravity $(x_{sc},z_{sc}) = (-0.30,1.77)$, indicated with a cross (×), is seen to be situated upstream of the central position $(x_l,z_n) = (0.0,1.8)$ of the laser beam, indicated with a dot (●).

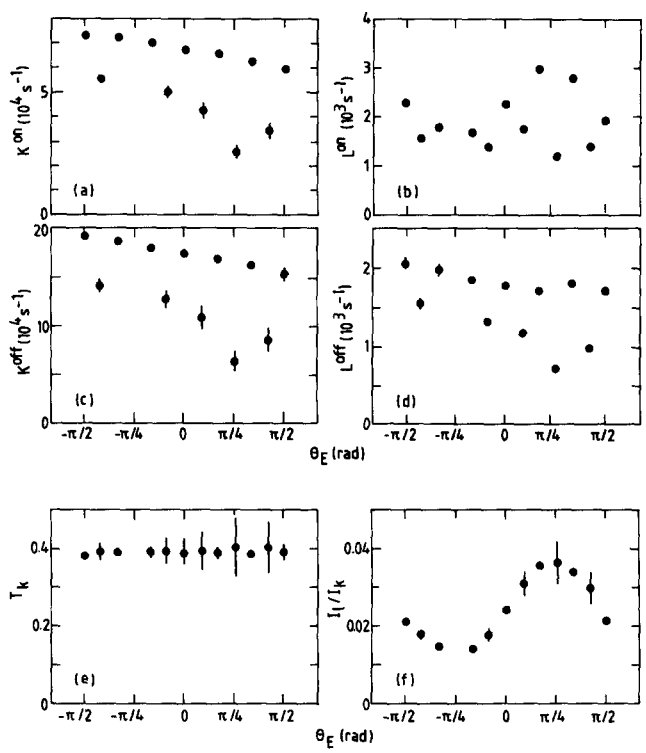

FIG. 26. The basic fluorescence signals K^{on} (a), L^{on} (b), K^{off} (c), and L^{off} (d) of Sec. IV A as a function of the laser polarization angle θ_E. These were measured with a stepsize of 30° in two series starting at −105° and −90°, respectively. The observed atypically large drift in time is seen to leave the derived results for the transmission T_k (e) of Eq. (7) and the ratio I_l/I_k (f) of Eq. (8) largely unaffected.

length of time, that the laser system can be counted on to maintain its stabilization on the transition frequency without a mode hop. If the laser were to fail during the experiment, or, e.g., a filter could not be located, the experimentalist is summoned to correct the problem. Of course, an entirely independent system of pressure-, temperature-, and coolant-water-flow monitors checks for problems of a different nature.

C. Types of measuring runs

The present "minibeam" experiment is concerned with the behavior of inelastic collision-induced cross sections $Q_{l\leftarrow k}$ as a function of the initial state $\{\alpha\}_k$, the final state $\{\alpha\}_l$, the collision energy E, the laser polarization angle θ_E, and the secondary-beam gas (He, Ne, N_2,...). A change of the initial state requires that the laser be tuned to a different transition frequency ν_{ik}, which takes time and calls for a human operator. An automated secondary-beam gas exchange system is being considered, but not operational. With these exceptions, all of the above variables can be changed during the measurements, by computer. However, in the interest of the subsequent analysis, it is generally wise to change only one variable at a time. Also, the more variables there are, the more prolonged a measurement will be, with a proportionally larger change of a problem developing.

We can distinguish between several basic types of measuring runs, examples of which will be given later in this section:

(1) Polarization measurement: I_l/I_k as a function of the polarization angle θ_E. The most fundamental measurement of all. In the case of an $|\alpha_k J_k = 1\rangle$ initial state, Eq. (21) indicates that two measurements suffice.

(2) Absolute scaling measurement: I_l/I_k for various final states $\{\alpha\}_l$, through a change of filters. The filter assembly takes up to four filter combinations at a time, in addition to the filters for the direct fluorescence. This type of measurement is very useful for calibrating a series of separate measurements.

(3) Energy measurement: I_l/I_k for different collision energies E. The change in energy is brought about by scanning the laser beam along the primary-beam axis. This results in a different direction of the secondary-beam velocity $\mathbf{v}_2$, and therefore in a different relative velocity g. The accessible energy range is limited, of course. A different, more laborious, means of changing the collision energy is through the use of a seeded primary beam, which directly affects the magnitude of the primary-beam velocity v_1. We have used various Ne/He mixtures.

(4) Time-of-flight measurement: I_l/I_k, resolved as to primary-beam velocity v_1. These measurements are very time consuming, even when using the pseudo-random correlation method mentioned in Sec. III. They are therefore best suited to strong transitions. Also, transitions with an $|\alpha_k J_k = 1\rangle$ initial state are favored over those with an $|\alpha_k J_k = 2\rangle$ initial state.

Used mainly for calibration purposes and therefore occupying a somewhat separate place is the following type of measurement:

(5) K-polarization measurement: the direct fluorescence signal K^{off} of Table III as a function of the polarization angle θ_E. This allows a check on the absence of a magnetic field. Also, it gives an idea of the sensitivity of the optical detection efficiency to the anisotropy of the fluorescence radiation emitted by polarized $\{\alpha\}_k$ atoms.

We repeat, that for measurements with a variety of secondary-beam gases (providing yet another cross section through variable space) to be in the same category as the above kinds of experiment, an adaptation of the gas-handling system would be required. A change in laser frequency, for another initial state $\{\alpha\}_k$, not only takes time in itself but may also affect laser-beam alignment. This calls for a repetition of the alignment procedure of Sec. III.

We will now present some results for the major types of experiments being performed. This is mostly by way of example. For a detailed analysis we refer to Refs. 20–22.

D. Polarized-atom cross sections

In Figs. 27–29 we show the experimental results $Q^{\beta}_{l\leftarrow k}$ for the Ne**–He $\{\alpha\}_5 \rightarrow \{\alpha\}_4$, $\{\alpha\}_6$, and $\{\alpha\}_7$ transitions, at center-of-mass energy $E \simeq 100$ meV.[20] The experiments were performed by pumping the $\{\alpha\}_5$ level through the $(^3P_0) \rightarrow \{\alpha\}_5$ transition at $\lambda = 626$ nm. The $\{\alpha\}_5$ state has $J_5 = 1$. We note that the whole gamut of possible polarization effects is observed. The $Q^{\beta}_{6\leftarrow 5}$ and $Q^{\beta}_{7\leftarrow 5}$ closely conform to the cos 2β expression of Eq. (21), as shown by the results of a least-squares fit of the data points. The somewhat deviating behavior of the $Q^{\beta}_{4\leftarrow 5}$ cross section is caused by the nonisotropic distribution of collision-induced fluorescence radiation, which takes on importance in the absence of a real polarization effect. It is possible to correct for this. We find that $Q^{|0|}_{l\leftarrow 5}/Q^{|1|}_{l\leftarrow 5} = 1.06, 0.52, 3.5$ for $l = 4$, 6, and 7, respectively. As to cross-section magnitude, the variation there is considerable as well, with $Q_{4\leftarrow 5}$ and $Q_{6\leftarrow 5}$ at opposite ends of the scale. Figure 30 of $Q^{\beta}_{8\leftarrow 9}$ at $E \simeq 100$ meV illustrates the presence of the higher order terms of Eq. (18). The data points were fitted with the model function of Eq. (18) for $n \leqslant 3$.

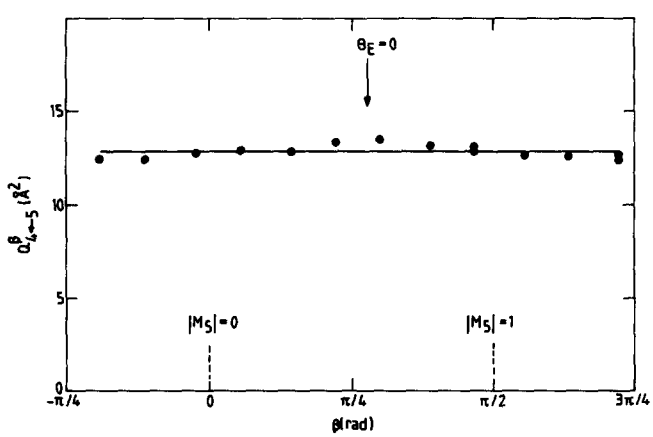

FIG. 27. Experimental results for the observed Ne**–He cross section $Q^{\beta}_{4\leftarrow 5}$ as a function of the angle β between the electric field E of the laser and the relative velocity g, at a center-of-mass energy $E_5 \simeq 100$ meV. The statistical errors are smaller than the size of the data points. The observed dependence on β reflects the nonisotropic distribution of fluorescence radiation, which we have not corrected for here. The drawn curve therefore indicates the average value of the data points and does not represent a curve fit according to Eq. (21).

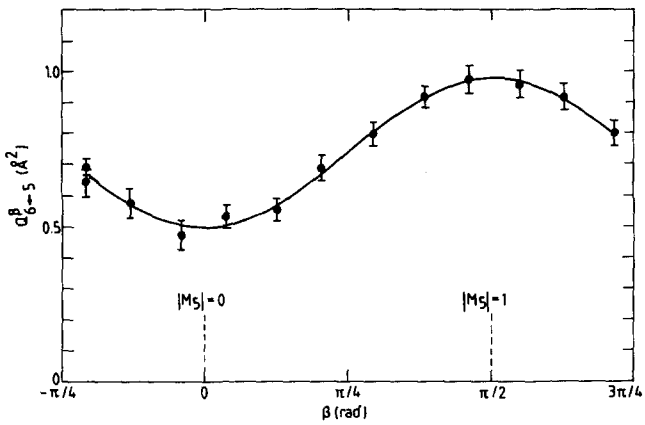

FIG. 28. Experimental results for the observed Ne**–He cross section $Q^{\beta}_{6\leftarrow5}$, as a function of the angle β between the electric field **E** of the laser and the relative velocity **g**, at a center-of-mass energy $E_5 \simeq 100$ meV. Statistical errors only have been indicated. The drawn curve represents a fit of the data points according to Eq. (21).

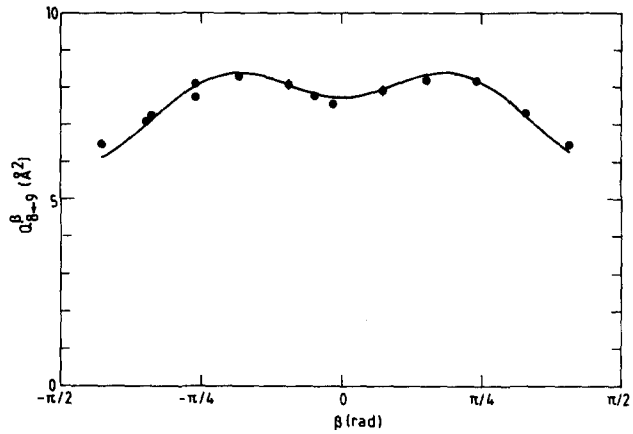

FIG. 30. Experimental results for the observed Ne**–He cross section $Q^{\beta}_{8\leftarrow9}$. Curve fit of data points according to Eq. (18) with $n<3$. See caption of Fig. 28 for further details.

The largest polarization effects observed so far are those for the Ne**–He $\{\alpha\}_7 \rightarrow \{\alpha\}_{4,5}$ transitions at $E \simeq 100$ meV with $Q^{|0|}_{l\leftarrow7}/Q^{|1|}_{l\leftarrow7} \simeq 0.1$ and 9 for $l = 4$ and 5, respectively.[21] For the $\{\alpha\}_7 \rightarrow \{\alpha\}_4$ transition we find a very small cross section $Q^{|0|}_{4\leftarrow7} \simeq 0.05$ Å^2. Compare this with the much larger Ne–CO_2 cross sections ($\simeq 50$ Å^2) shown in Sec. V F.

E. Energy dependence

The observed energy dependence of the $Q^{|M_5|}_{4\leftarrow5}$ and $Q^{|M_5|}_{7\leftarrow5}$ cross sections for Ne**–He is shown in Figs. 31 and 32.[20,21] The measurements have been performed both by varying the magnitude of the primary beam velocity $\mathbf{v}_1$ (by using a 15% Ne–85% He seeded primary beam) and by varying the direction of the secondary-beam velocity $\mathbf{v}_2$ (by scanning the laser beam along the primary-beam axis). In general, the energy range that is accessible by these means is $50 \lesssim E \lesssim 250$ meV (depending to some extent on the secondary-beam gas).

Velocity-averaged results only are presented here. The actual velocity distribution in the scattering center matters relatively little for these transitions, but plays an important role, in, e.g., the highly endothermic $\{\alpha\}_7 \rightarrow \{\alpha\}_5$ transition,

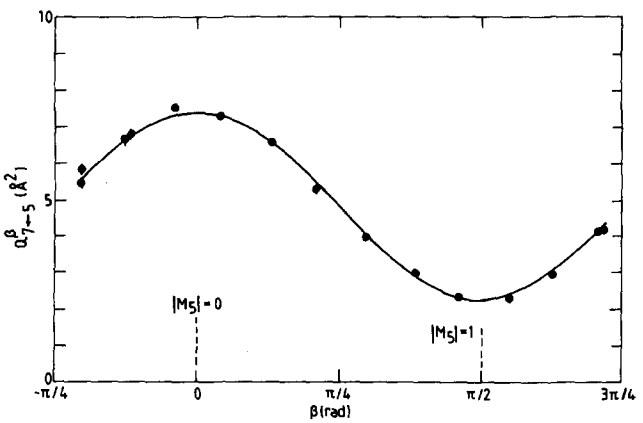

FIG. 29. Experimental results for the observed Ne**–He cross section $Q^{\beta}_{7\leftarrow5}$. See caption of Fig. 28 for further details.

where the energy threshold is $\Delta E_{57} = 81$ meV. This effect becomes progressively less important at higher energies.

In time-of-flight (TOF) measurements, the separate TOF spectra of the K^{off}, K^{on}, L^{off}, and L^{on} signals (see Sec. IV) can be combined into an I_l/I_k spectrum in the usual fashion [i.e., in accordance with Eq. (8)]. In theory, continuous coverage of the thermal velocity range is possible by performing TOF measurements at various laser-beam positions (as in the energy measurements, discussed earlier). Some preliminary results, applying to the Ne**–He $\{\alpha\}_5 \rightarrow \{\alpha\}_7$ transition for $|M_5| = 0$, can be seen in Fig. 33.The pseudo-random correlation method was employed here, with a channel time $t_k = 5$ μs, at three different laser positions. Unfortunately, deconvolution along the lines of Sec. IV [Eq. (10)], undertaken separately for each primary-beam velocity, not quite succeeds in achieving the desired overlap of cross-section values, yet.

F. System-related aspects

The minibeam apparatus described in the present paper was set up specifically for experiments with short-lived Ne**

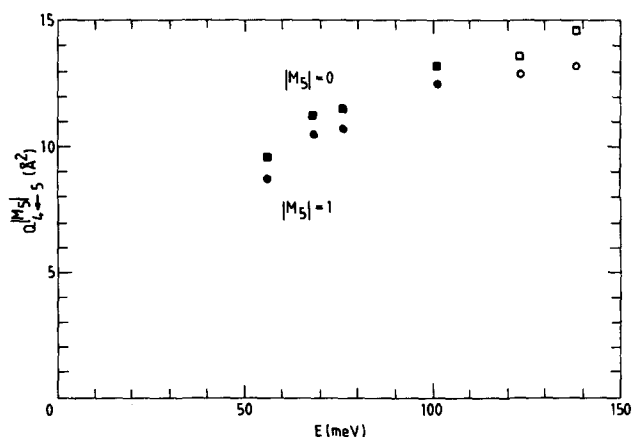

FIG. 31. Energy dependence of the polarized Ne**–He cross sections $Q^{|0|}_{4\leftarrow5}$ and $Q^{|1|}_{4\leftarrow5}$, with E the center-of-mass energy. The open points have been obtained by varying the magnitude of the primary-beam velocity $\mathbf{v}_1$; the full points by varying the position of the laser beam along the primary-beam axis, and thus the direction of $\mathbf{v}_2$.

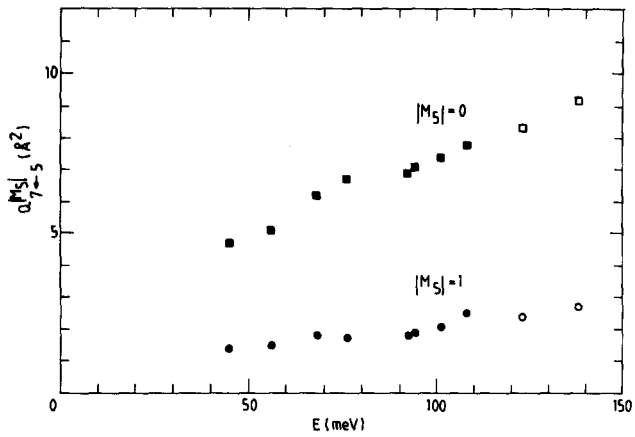

FIG. 32. Energy dependence of the polarized Ne**–He cross sections $Q^{|0|}_{7\leftarrow 5}$ and $Q^{|1|}_{7\leftarrow 5}$. See caption of Fig. 31 for further details.

atoms. A change to a different noble gas atom such as Ar** or Kr**, while highly interesting, entails certain practical difficulties.

The production of metastable atoms is not one of these. The metastale beam source will accommodate a variety of noble gases. As to the optical detection system, this would require at least a new set of interference filters and probably a different type of photomultiplier as well. It is, however, the need for a laser operating in a different wavelength region that presents the major (financial) problem. In our laboratory, work on diode lasers is in progress, which will perhaps make the transition to Ar** or Kr** a viable option.

As opposed to the situation for the short-lived atom, there is a wide choice in ground-state collision partners. Generally speaking, only corrosive gases are excluded, for obvious reasons. Noble gas atoms from Ar upwards offer the chance of an indirect view of Penning ionization, a process not occurring for the Ne**–He and Ne**–Ne systems we have so far concentrated on. In Ne**–molecule collisions, processes like angular momentum coupling and rotational excitation must be considered (as they must in, e.g., Ne–H_2 collisions[39]), in addition to intramultiplet mixing and Penning ionization.

We have performed preliminary measurements for Ne**–Ar, Kr, Xe and for Ne**–H_2, CH_4, N_2, CO_2, N_2O. By way of example, Figs. 34 and 35 show the observed cross sections $Q^{\beta}_{7\leftarrow 5}$ for Ne**–CO_2 and Ne**–N_2O, respectively, at approximate energy $E = 160$ meV. We note first that in both cases the polarization effect is smaller than for Ne**–He (compare Fig. 29). This is part of a general trend. Remarkably, the polarization effect is reversed for Ne**–CO_2. Also, there is a large difference in cross section magnitude. Anisotropy effects are expected to play an important role here. To derive from experimental data such as these information about the interactions constitutes a major challenge.

VI. CONCLUDING REMARKS

The minibeam experiment, described in these pages, has proven to be a valuable instrument for the study of inelastic collisions of short-lived Ne** atoms. With some exaggeration, it can be said to combine the sensitivity of a beam-gas cell experiment with the resolution of a full-size crossed-beam experiment. The disadvantages attached to the use of a free-jet secondary-beam expansion (alignment problems on the one hand, convolution difficulties in the calibration on the other) are surmountable. The possibility of varying the collision energy by moving the scattering center position is a bonus in this respect.

In the near future we will install a hollow cathode arc metastable beam source,[40] thus opening up the superthermal energy range $0.5 < E < 5$ eV, as well. At the same time, cooling and/or heating of the secondary-beam nozzle should be relatively easy to achieve. In this regard, we note that a laterally movable nozzle assembly would significantly enhance the capacity for energy variation by manipulation of the Newton diagram of the primary- and secondary-beam velocity vectors. In the longer term, the availability of diode lasers operating in the infrared raises the prospect of experiments with short-lived Ar** or Kr** atoms.

Diode lasers might also be used in combination with the present dye laser in a two-photon-excitation experiment. In

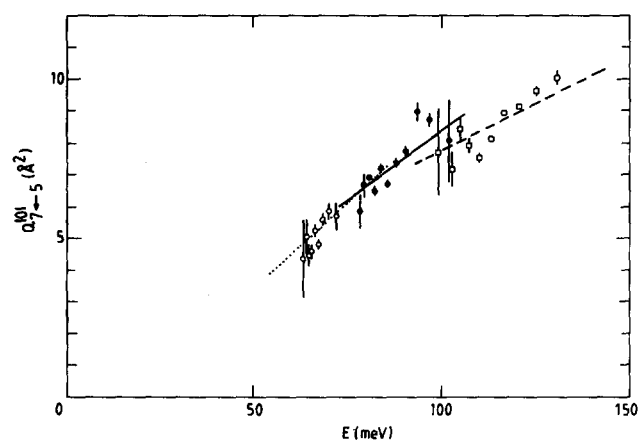

FIG. 33. Energy dependence of the polarized Ne**–He cross sections $Q^{|0|}_{7\leftarrow 5}$, obtained from time-of-flight measurements at three different laser-beam positions. Together these measurements span the $60 \lesssim E \lesssim 140$ meV energy range. The TOF data were obtained using the pseudo-random correlation method, with a channel time $t_k = 5\ \mu$s. The lines in the figure are the result of the velocity-dependent deconvolution. Their overlap still leaves something to be desired.

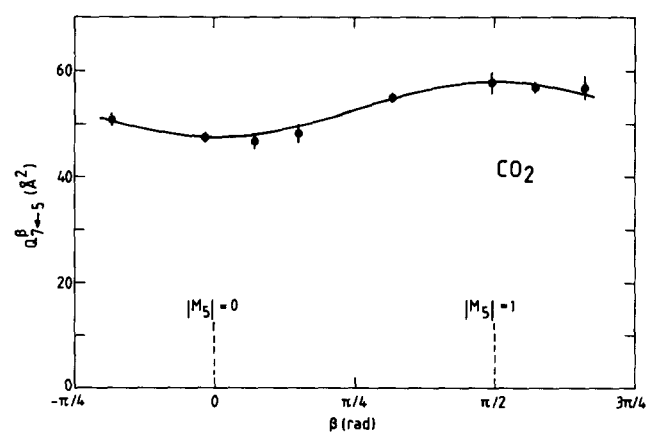

FIG. 34. Experimental results for the observed Ne**–CO_2 cross section $Q^{\beta}_{7\leftarrow 5}$, at energy $E_5 \simeq 160$ meV. See caption of Fig. 28 for further details. Note the differences with Fig. 35.

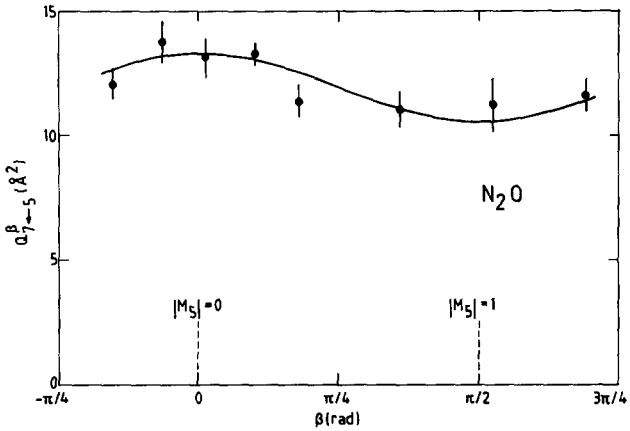

FIG. 35. Experimental results for the observed Ne**–N_2O cross section Q^{β}_{7-5}, at energy $E_5 \simeq 160$ meV. See caption of Fig. 28 for further details. Note the differences with Fig. 34.

this, the short-lived two-level system $\{\alpha\}_9$ state, produced by the dye laser in a saturated transition from the metastable ($^3P_2$) state, would be excited by the diode laser to the lowest Rydberg-type states.

The large polarization effects that are observed attest to the interest of the Ne**–atom/molecule systems. For a system like Ne**–He in particular, the experiment provides the invaluable first ingredient for a complete analysis of interaction and collision dynamics. The fortunate availability of Ne**–He model potentials is another such ingredient. Using quantum-mechanical coupled-channels calculations,[20] supplemented where possible by semiclassical calculations,[21] a direct confrontation between theory and experiment has become possible.

[1]D. Hennecart and F. Masnou-Seeuws, J. Phys. B **18**, 657 (1985).
[2](a) W. Buszert, T. Bregel, R. J. Allan, M.-W. Ruf, and H. Hotop, Z. Phys. A **320**, 105 (1985); (b) W. Buszert, T. Bregel, J. Ganz, K. Harth, A. Siegel, M.-W. Ruf, H. Hotop, and H. Morgner, J. Phys. (Paris) **46**, C19 (1985).
[3]M. H. Alexander, T. Orlikowski, and J. E. Straub, Phys. Rev. A **28**, 73 (1983).
[4]G. Nienhuis, Phys. Rev. A **26**, 3137 (1982).
[5]J. G. Kircz, R. Morgenstern, and G. Nienhuis, Phys. Rev. Lett. **48**, 610 (1982).
[6]H. A. J. Meyer, H. P. van der Meulen, and R. Morgenstern, Z. Phys. D **5**, 299 (1987).
[7]D. Neuschäfer, M. O. Hale, I. V. Hertel, and S. R. Leone, in *Electronic and Atomic Collisions*, edited by D. C. Lorents, W. E. Meyerhof, and J. R. Peterson (Elsevier, Amsterdam, 1986).
[8](a) M. O. Hale, I. V. Hertel, and S. R. Leone, Phys. Rev. Lett. **53**, 2296 (1984); (b) M. O. Hale and S. R. Leone, Phys. Rev. A **31**, 103 (1985).
[9]J. M. Parson and T. Ishikawa, J. Chem. Phys. **80**, 3137 (1984).
[10]A. Bähring, I. V. Hertel, E. Meyer, W. Meyer, N. Spies, and H. Schmidt, J. Phys. B **17**, 2859 (1984).
[11](a) D. Hennecart, J. Phys. (Paris) **39**, 1065 (1978); (b) Ph.D. thesis, Université de Caen, 1982 (unpublished).
[12]J. M. Mestdagh, J. Berlande, P. de Pujo, J. Cuvallier, and A. Binet, Z. Phys. A **304**, 3 (1982).
[13]E. Düren, E. Hasselbrink, and H. Tischen, Phys. Rev. Lett. **50**, 1983 (1983).
[14]L. Hüwel, J. Maier, and H. Pauly, J. Chem. Phys. **76**, 4961 (1982).
[15]H. J. Yuh and P. J. Dagdigian, Phys. Rev. A **28**, 63 (1983).
[16](a) N. Böwering, M. R. Bruce, and J. W. Keto, J. Chem. Phys. **84**, 709 (1986); (b) **84**, 715 (1986).
[17]J. K. Kuh and D. W. Setser, J. Chem. Phys. **84**, 4304 (1986).
[18]I. V. Hertel, H. Schmidt, A. Bähring, and E. Meyer, Rep. Prog. Phys. **48**, 375 (1985).
[19]M. P. I. Manders, J. P. J. Driessen, H. C. W. Beijerinck, and B. J. Verhaar, Phys. Rev. Lett. **57**, 1577, 2472 (1986).
[20]M. P. I. Manders, J. P. J. Driessen, H. C. W. Beijerinck, and B. J. Verhaar, Phys. Rev. A **37**, 3237 (1988).
[21]M. P. I. Manders, W. B. M. van Hoek, E. J. D. Vredenbregt, G. J. Sandker, H. C. W. Beijerinck, and B. J. Verhaar (to be published).
[22]M. P. I. Manders, W. Boom, H. C. W. Beijerinck, and B. J. Verhaar (to be published).
[23]J. P. C. Kroon, Ph.D. thesis, Eindhoven University of Technology, 1985.
[24]M. J. Verheijen, H. C. W. Beijerinck, L. H. A. M. van Moll, J. P. J. Driessen, and N. F. Verster, J. Phys. E **17**, 904 (1984).
[25]H. C. W. Beijerinck and N. F. Verster, Physica C **111**, 327 (1981).
[26]M. J. Verheijen, H. C. W. Beijerinck, and N. F. Verster, J. Phys. E **15**, 1198 (1982).
[27]J. P. C. Kroon, H. C. W. Beijerinck, B. J. Verhaar, and N. F. Verster, Chem. Phys. **90**, 195 (1984).
[28]M. J. Verheijen, H. C. W. Beijerinck, and N. F. Verster, Rev. Sci. Instrum. **56**, 62 (1985).
[29](a) H. C. W. Beijerinck, R. J. G. M. Moonen, and N. F. Verster, J. Phys. E **7**, 31 (1974); (b) H. C. W. Beijerinck, Ph.D. thesis, Eindhoven University of Technology, 1975.
[30]S. M. Trujillo, P. K. Rol, and E. W. Rothe, Rev. Sci. Instrum. **33**, 841 (1962).
[31]A. W. F. van Gerven, Int. Rep. TUE VDF/NO 86-16 (1986) (in Dutch).
[32]F. C. van Nijmwegen, Int. Rep. TUE VDF/CO 84-09 (1984) (in Dutch).
[33]P. W. E. Verhelst and N. F. Verster, Software Practice and Experience **14**, No. 2, 119 (1984).
[34]F. C. van Nijmwegen, Int. Rep. TUE FTI/BA 87-03 (1987) (in Dutch).
[35]J. H. Voskamp, F. C. van Nijmwegen, and J. M. P. van Erum, Conference Proceedings Computing in High Energy Physics, edited by L. O. Hertzberger and W. Hoogland (1986), p. 222.
[36]I. S. Gradshteyn and I. M. Ryzhik, *Tables of Integrals, Series, and Products* (Academic, New York, 1965).
[37]H. C. W. Beijerinck, Comments At. Mol. Phys. **19**, 227 (1987).
[38]A. Messiah, *Quantum Mechanics* (North-Holland, Amsterdam, 1981), Vols. I,II.
[39]J. Robert, V. Bocvarski, B. Stern, J. Reinhardt, and J. Baudon (to be published).
[40]P. G. A. Theuws, H. C. W. Beijerinck, D. C. Schram, and N. F. Verster, J. Phys. E **15**, 573 (1982).